AIP | Journal of Applied Physics

Ignition criterion for heterogeneous energetic materials based on hotspot size-temperature threshold

A. Barua, S. Kim, Y. Horie, and M. Zhou

Citation: J. Appl. Phys. **113**, 064906 (2013); doi: 10.1063/1.4792001
View online: http://dx.doi.org/10.1063/1.4792001
View Table of Contents: http://jap.aip.org/resource/1/JAPIAU/v113/i6
Published by the American Institute of Physics.

JOURNAL OF APPLIED PHYSICS **113**, 064906 (2013)

Ignition criterion for heterogeneous energetic materials based on hotspot size-temperature threshold

A. Barua,[1] S. Kim,[1] Y. Horie,[2,a)] and M. Zhou[1,b)]
[1]*The George W. Woodruff School of Mechanical Engineering, School of Materials Science and Engineering, Georgia Institute of Technology, Atlanta, Georgia 30332-0405, USA*
[2]*Air Force Research Lab, Munitions Directorate, 2306 Perimeter Road, Eglin AFB, Florida 32542, USA*

(Received 19 August 2012; accepted 28 January 2013; published online 13 February 2013)

A criterion for the ignition of granular explosives (GXs) and polymer-bonded explosives (PBXs) under shock and non-shock loading is developed. The formulation is based on integration of a quantification of the distributions of the sizes and locations of hotspots in loading events using a cohesive finite element method (CFEM) developed recently and the characterization by Tarver *et al.* [C. M. Tarver *et al.*, "Critical conditions for impact- and shock-induced hot spots in solid explosives," J. Phys. Chem. **100**, 5794–5799 (1996)] of the critical size-temperature threshold of hotspots required for chemical ignition of solid explosives. The criterion, along with the CFEM capability to quantify the thermal-mechanical behavior of GXs and PBXs, allows the critical impact velocity for ignition, time to ignition, and critical input energy at ignition to be determined as functions of material composition, microstructure, and loading conditions. The applicability of the relation between the critical input energy (E) and impact velocity of James [H. R. James, "An extension to the critical energy criterion used to predict shock initiation thresholds," Propellants, Explos., Pyrotech. **21**, 8–13 (1996)] for shock loading is examined, leading to a modified interpretation, which is sensitive to microstructure and loading condition. As an application, numerical studies are undertaken to evaluate the ignition threshold of granular high melting point eXplosive, octahydro-1,3,5,7-tetranitro-1,2,3,5-tetrazocine (HMX) and HMX/Estane PBX under loading with impact velocities up to 350 ms^{-1} and strain rates up to 10^5 s^{-1}. Results show that, for the GX, the time to criticality (t_c) is strongly influenced by initial porosity, but is insensitive to grain size. Analyses also lead to a quantification of the differences between the responses of the GXs and PBXs in terms of critical impact velocity for ignition, time to ignition, and critical input energy at ignition. Since the framework permits explicit tracking of the influences of microstructure, loading, and mechanical constraints, the calculations also show the effects of stress wave reflection and confinement condition on the ignition behaviors of GXs and PBXs. © *2013 American Institute of Physics*. [http://dx.doi.org/10.1063/1.4792001]

I. INTRODUCTION

The issue of impact-induced ignition in energetic materials has received significant attention over the past few decades.[1–6] Ignition can occur as a result of energy localization in the form of local temperature increases or hotspots. A number of thermomechanical processes occur simultaneously subsequent to impact loading, and it is not straightforward to ascribe the ignition to one particular cause.[7] Impact-induced-initiation can be roughly divided into two regimes of interest: shock and non-shock conditions. A brief survey of the most relevant work in both shock and non-shock loading is provided here.

Shock loading is one type of mechanical insults that can result in initiation and detonation.[8,9] There has been significant progress in developing empirical threshold criteria for ignition under shock loading. In 1969, Walker and Wasley[10] introduced a critical energy relation to describe shock ignition of select solid explosives. This relation, commonly referred to as $P^2\tau = \text{constant}$, relates the energy flux of a sustained plane shock to ignition. The relation was found, however, to be limited in terms of the range of conditions applicable and the number of materials which obey it. Proceedings of the Detonation Symposium (particularly the 7th) contain numerous attempts at establishing shock thresholds in terms of shock wave parameters.

Recently, James[2] generalized the $P^2\tau = \text{constant}$ relation by including a specific energy "cutoff" analogous to an activation energy. The modification is significant since it allowed the relation to be extended to both homogeneous and heterogeneous explosives.

Several researchers have focused on computational modeling of shock ignition. Relevant works include the modeling of heterogeneous microstructures at the mesoscale (Baer[3,11,12] and Benson *et al.*[13,14]), shock response of porous explosives (Hayes[15]), compaction of granular high melting point eXplosive, octahydro-1,3,5,7-tetranitro-1,2,3,5-tetrazocine (HMX) (Menikoff[16,17]), chemical reaction and hotspot formation (Dlott[18,19]), micromechanical burn of solid explosives (Hamate and Horie[6]), and chemical kinetics of reaction in pure explosives (Tarver *et al.*[1] and Henson *et al.*[20]), among others.

In the case of non-shock loading, the stress wave front is more diffused. Experimental evidence from Idar[21] suggests

a)Retired.
b)Electronic mail: min.zhou@gatech.edu.

that the processes associated with non-shock loading occur over a time span of several microseconds to even milliseconds. Such loads allow slower mechanisms to play a role, including rearrangement of grains and possibly heat loss from hotspots to a cooler region. The dominating energy dissipation mechanisms in non-shock ignition are thought to be friction, followed by plasticity and viscous flow. The failure mechanisms are also significantly affected by the temperature and strain rate (Gray *et al.*[22]).

In terms of modeling, Dienes *et al.*[23] studied the impact initiation of explosives using statistical crack mechanics. This approach accounts for crack growth and coalescence. Frictional heating caused by sliding of crack faces can also be analyzed. The authors showed that the overall load displacement response using the approach matches well with experimental results. However, since microstructure is not considered, the spatial distribution of quantities is not captured explicitly.

More recently, Gonthier *et al.*[24] performed mesoscale simulations of impact loading of granular explosives (GXs). The model accounts for effects of inter-granular friction and plasticity. Such simulations can be used to predict the temperature distribution in the materials as a function of loading and microstructural parameters. Barua *et al.*[25–27] developed a novel capability based on the cohesive finite element method (CFEM) for analyzing the thermal and mechanical responses of heterogeneous energetic materials including polymer-bonded explosives (PBXs) and GXs. The framework provides explicit account of material microstructure, coupled thermal-mechanical kinetics, elastic-viscoelastic-elasto-plastic constitutive behaviors, fracture, and frictional heating. Wu *et al.*[28] focused on developing an initiation model using relations between macroscopic variables and conditions at intergranular contact areas. An early effort by Browning[29] is unique in that he developed an analytical threshold condition by combining heat conduction equation with chemical kinetics and sliding friction in both one and two space dimensions.

The challenge associated with the study of ignition in non-shock loading is that the thermal-mechanical-chemical processes may occur over time spans of a few microseconds to several milliseconds. The initiation of chemical reaction is significantly affected by the local fluctuations of field quantities, which depend on both microstructural heterogeneity and loading. Most importantly, the response cannot simply be quantified by one (such as pressure in the case of shock loading) or a small number of parameters. Specifically, the issue partly relates to the formation of hotspots whose temperatures, sizes, morphologies, and proximities depend on

(1) not only the hydrostatic part of the stress tensor but also the deviatoric part of the stress tensor (i.e., stress triaxiality);
(2) not only the volumetric responses but more importantly the shear response of the materials;
(3) thermal conduction; and
(4) microstructure.

There is also a common thread for both shock and non-shock loading. In both cases, it is the hotspots that, once formed, serve as ignition sites and react exothermally. Therefore, hotspots determine the stability of the GXs or the PBXs. The significant effect of loading conditions on the evolution and spatial distribution of hotspots under non-shock loading conditions has been well established.[26]

The goal of this work is to develop an ignition criterion based on the conditions of mechanical loading and microstructural attributes. We accomplish this by considering the two phenomena, hotspot generation and local temperature evolution under influence of chemical reactions, as separate but related processes.

The former is concerned with the quantification of the contributions of different dissipation/heating mechanisms and how the contributions evolve as deformation progresses. This task is achieved through use of a recently developed Lagrangian cohesive finite element framework to quantify the effects of microstructure and thermal-mechanical processes, such as matrix deformation, interfacial debonding, and fracture of grains on hotspot formation. Simulations are carried out for a range of strain rates, microstructure, and loading conditions for both GX and PBX. The details of the theoretical framework used are published in Ref. 25.

The latter (thermo-chemical runaway) is solved independent of hotspot dynamics—they are in essence "borrowed" from the existing work. The seminal work in this area was done in the 1920s by Semenov[30] and later by Kamenetskii.[31] Semenov[30] developed a criticality model, which was a solution of the heat diffusion equation with heat generation due to reaction. Frank-Kamenetskii worked on the same heat conduction equation but with varying temperature distribution. Thomas[32] developed a unifying model, which incorporated the elements of both Semenov and FK's work. Together, this and other works (e.g., Gray[33,34] and Boddington[35,36]) provided an analytical approach for obtaining the critical size of hotspots required for ignition as a function of temperature. The critical hotspot-size combinations form the threshold that can be taken as a material attribute. Such threshold relations can also be obtained using chemical kinetics calculations.[1,20] It must be cautioned, however, that in this paper, we are not tackling the issue of subsequent burn after ignition, which may result in detonation of explosives.

In summary, the objective of this work is to connect locally heated high temperature spots due to thermal-mechanical processes to the ignition process defined as the thermal run-away phenomenon in the localized high temperature regions. The ultimate goal is to understand and quantify the mechanisms leading to initiation in energetic materials. The analysis will help create microstructure-performance maps for the development of PBXs with tailored attributes. We are mindful of the need to validate the model calculations, but have not yet found data from well-defined comparable experiments with well-characterized microstructures. Hopefully, this paper will serve as a stimulus for such experiments to be conducted in the near future.

II. IGNITON CRITERION

Mathematically, the criterion at the junction of the first (thermal-mechanical) phenomenon which provides hotspots

and the second (thermal-chemical) phenomenon which leads to thermal runaway can be stated as

$$d(T) \geq d_c(T), \tag{1}$$

where, d is the diameter of the dominant hotspot resulting from a loading event whose interior temperatures are at or above temperature T and d_c is the minimal diameter of a hotspot required for thermal runaway at temperature T. Note that the right-hand side of Eq. (1) represents the boundary between "ignition" and "non-ignition" in the $d-T$ space and reflects material attributes. Information about this material properties part of the criterion has to be obtained independently, from experiments or thermal-chemical calculations. In the current paper, this information comes from hotspot size-temperature threshold relations for solid explosives derived from thermal-chemical reaction calculations. The rest of this paper focuses on the two sides of the criterion in Eq. (1), first the right-hand side, then the left-hand-side. It is important to point out at the outset that because the hotspot state represented on the left hand side of Eq. (1) can be the result of either shock or non-shock loading and the thermal-chemical threshold condition embodied on the right hand side of Eq. (1) is independent of loading, the criterion proposed here should in general apply to both non-shock and shock loading. However in this paper, the analyses solely concern non-shock conditions. The application to shock loading can be discussed separately with appropriate computational and experimental data in the future.

A. Thermal criticality threshold

At present, hotspot sizes and temperatures cannot be measured experimentally. Hence, we need to rely on theoretical estimates to predict thermal criticality of hotspots. Criticality occurs when the temperature in a hotspot of a given size and shape is high enough so that the rate of temperature increase due to chemical reaction is higher than the rate of temperature decrease due to heat loss through conduction (and other dissipative processes if any) across the surface of the hotspot. The thermal criticality threshold is used to relate the size and temperature of hotspots at the critical condition in Eq. (1). Solutions of the heat diffusion equation with heat generation due to reaction have been used to predict the temperature rise in hotspots for a range of canonical shapes (spherical, planar circular, elliptical, etc.). The analytical formulation can be expressed as[7]

$$d_c = f(T_s, \text{material properties}, \text{shape}), \tag{2}$$

where T_s is the temperature at the surface of the hotspot. The specific form of Eq. (2) obtained from the solution of the heat diffusion equation is presented in *Non-shock Initiation of Explosives*, p. 202.[7] The relation considers pure explosive materials following single-step Arrhenius reaction kinetics and is independent of the loading conditions (shock or non-shock). In summary, the analytical formulation can be used to estimate the critical size of a hotspot with a specific shape, at a given surface temperature.

Tarver *et al.*[1] performed chemical kinetics calculations to analyze the criticality issue for HMX and 2,4,6-triamino-1,3,5- trinitrobenzene explosives. The calculations consider multistep reaction mechanisms and the pressure and temperature dependence of reactants and products. The black line in Fig. 1 shows the calculated critical temperature as a function of size for spherical hotspots in HMX.[1] For comparison, the analytical formulation as fitted to Tarver *et al.*'s data [Eq. (2)] from Ref. 7 for a spherical hotspot is also plotted in Fig. 1 (red line). The fit provides a good description of Tarver *et al.*'s data.[1] This is of interest since Tarver *et al.*[1] considered a three-step reaction pathway for the decomposition of HMX. The close agreement with the analytical response suggests that over this range of ignition times, there could be a single rate-limiting step in the ignition mechanism.

It must be noted that Henson[20] suggested a similar possibility since the data for ignition time as a function of temperature appears to be close to linear on the log-log scale. Specifically, he also performed chemical kinetics calculations and came up with a critical size vs. temperature relationship for hotspots in HMX, which is shown in Fig. 1 in blue. The disparity between the results from Tarver *et al.*[1] and Henson[20] may stem from the way in which the hotspot temperatures are calculated. In this paper, the relation provided by Tarver *et al.*[1] is used to identify critical hotspots. It is noted that, although there is a numerical difference in the relations provided in Refs. 1 and 20, the qualitative nature and the trend of the response are be similar regardless of which set of data is used.

B. Microstructure-level model

The finite element framework uses linear triangular bulk elements, which are interspaced by 4−noded cohesive elements. These cohesive elements are distributed throughout the mesh at all bulk element interfaces. The cohesive elements follow a traction-separation law relating the traction

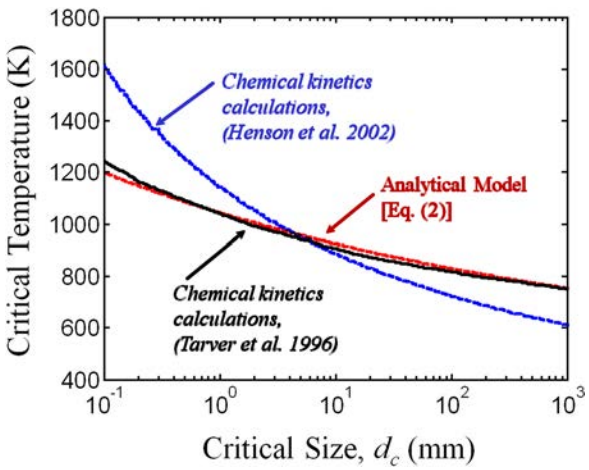

FIG. 1. Temperature-hotspot size threshold curves for ignition or thermal runaway of HMX, data from chemical kinetics calculations performed by Tarver *et al.*[1] (used in the analyses of this paper) is shown, along with the analytical relation in Eq. (2), which is fitted to Tarver *et al.*'s data. For comparison, Henson's[20] data are also shown, but not used in the material-specific analyses of this paper.

on the cohesive surface pair to the interfacial separation. The bilinear traction-separation law developed by Zhai and Zhou[37,38] is used in case of tensile and shear separations. Under compression, a penalty traction is used to strongly discourage interpenetration of cohesive surfaces. Failure of cohesive elements results in the creation of new surfaces, which represent cracks. To prevent interpenetration of the crack faces, a contact algorithm is used to apply a normal penalty force to prevent the overlap of elements. The Coulomb friction law is used to determine the frictional force between contacting surface pairs. Heating due to friction is accounted for, along with dissipation from bulk plasticity and viscoelasticity.

The finite element discretization is based on linear-displacement triangular elements arranged in a crossed-triangle quadrilateral pattern. The element size chosen is 15 μm based on a convergence study performed in Ref. 25. The finite element size limits the lowest resolution of hotspots that can be identified using this analysis. Specifically, hotspot sizes detected are approximately on the order of 40–50 μm, depending on the threshold temperature, microstructure, and loading conditions. The dominant hotspots (those that determine ignition) have sizes on the order of 40–50 μm. Finite element sizes smaller than what is used may provide slightly better resolution of the hotspots, but also significantly increase calculation time. Adaptive meshing can be used to improve resolution at large deformations in the future.

The binder is modeled using a finite deformation viscoelastic model. A 22-element Prony series from Ref. 39 is used to characterize the variation of the shear modulus with the relaxation time. For the HMX granules, a hyperelastic constitutive model is used. Since the cohesive elements are embedded throughout the entire finite element mesh at all bulk element interfaces, arbitrary crack/microcrack patterns are resolved. Specifically, fracture of the grains, debonding at the grain/matrix interfaces, and tearing of the binder can be tracked explicitly. This study focuses on non-shock conditions, therefore, the HMX grains undergo very little plastic deformation, justifying the use of a hyperelastic model for the bulk deformation and a cohesive traction separation law to model the fracture of grains. The constitutive parameters for HMX, Estane, and the cohesive interface properties are given in Ref. 25.

C. Statistical characterization of hotspot field using radial distribution function (RDF)

The size and temperature of hotspots need to be quantified prior to the application of any threshold criteria for ignition. In a previous work,[26] the authors employed a method to identify hotspots, which involves a circular "microscope" sweeping through the microstructure to identify potential hotspots. That scheme requires a rigid criterion for identifying hotspots and does not lend itself to systematic quantification of the distribution of hotspot size.

To avoid the use of arbitrary size-temperature criteria in identifying hotspots, a novel scheme is developed here. This new approach involves the use of a temperature threshold (ΔT_{thres}), which is of vital importance. At each time step, the microstructure is scanned for temperature rises above ΔT_{thres}. Areas of a temperature field with temperatures above the threshold are analyzed for hotspots. Successively varying ΔT_{thres} values allows the characteristics of a temperature field to be fully analyzed. In particular, strategically chosen threshold temperature values allow hotspots of interest to be identified.

To illustrate how this scheme works, Fig. 2(a) shows an idealized regular array of circular hotspots, each having a temperature rise of 50 K at the center and 0 K at the periphery. The variation of temperature inside the hotspots follows

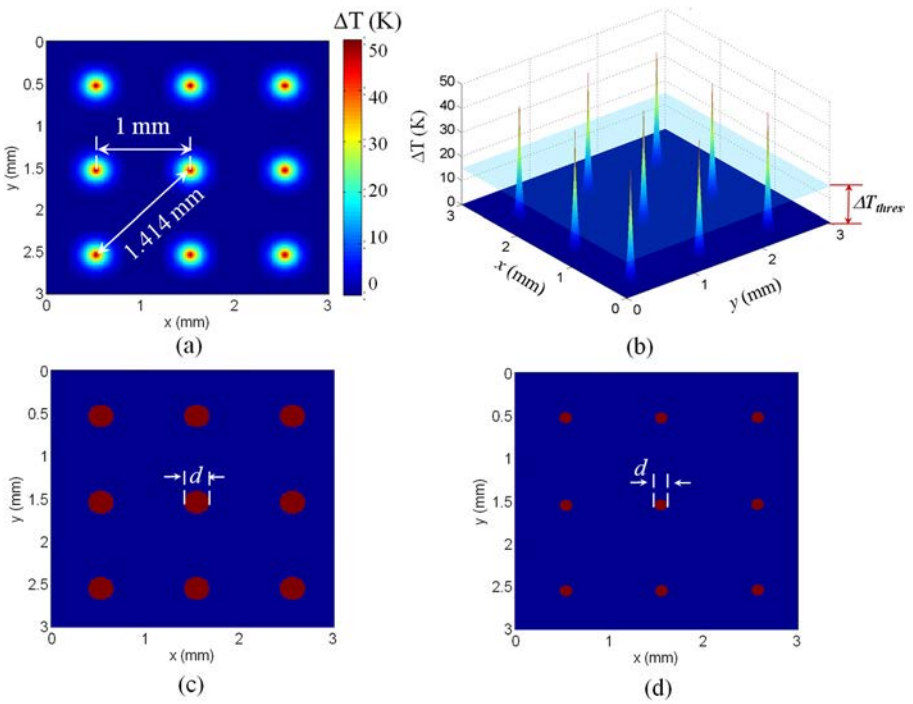

FIG. 2. Illustration and quantification of an idealized hotspot field, (a) hotspots arranged in a regular square array, (b) 3D temperature profile of the idealized hotspots field, and a schematic sectioning of the hotspot field by a plane at a given cutoff temperature, ΔT_{thres}, (c) hotspots on section with $\Delta T_{thres} = 15$ K,and (d) hotspots on section with $\Delta T_{thres} = 30$ K.

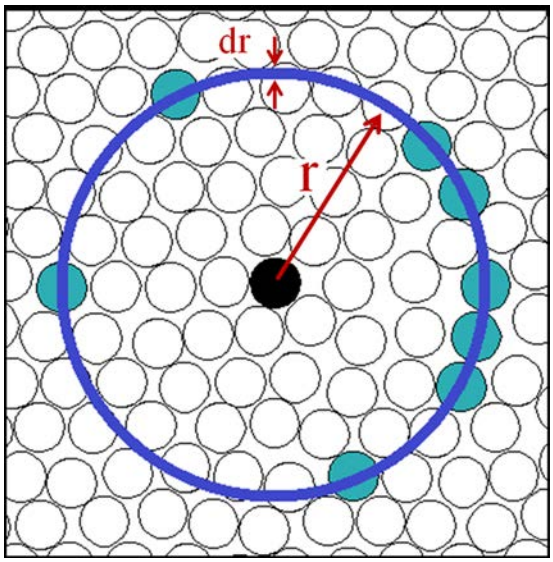

FIG. 3. Schematic illustration of the RDF.

a smooth polynomial function. Figure 2(b) shows a 3D visualization of the temperature field with temperature as the vertical axis. A plane representing a threshold temperature of $\Delta T_{thres} = 15$ K is shown intersecting the hotspot fields. Obviously, varying this ΔT_{thres} would reveal the hotspots and allow them to be quantified in different ways. Figures 2(c) and 2(d) show the hotspot fields obtained by using $\Delta T_{thres} = 15$ and 30 K, respectively. These quantifications can be further analyzed to obtain more detailed statistical information.

The RDF is used as a measure to statistically characterize the spatial distribution of hotspots. Historically, the RDF has been used extensively to analyze the arrangement of atoms and molecules,[40,41] packing of spheres,[42] and solidification and structure of metals.[43] As illustrated in Fig. 3, the RDF describes how the density of a system of particles varies as a function of interparticle distance. Specifically, the RDF $f(r)$ represents the probability of finding a particle in a shell with thickness dr at a distance r from a particle. The number of particles $dn(r)$ at a distance between r and $r + dr$ from a given particle is

$$dn(r) = \rho \cdot f(r) \cdot 4\pi r^2 dr, \tag{3}$$

where $\rho = N/V$ is the average density of particles in the system, with N the total number of particles in the system with total volume V. The above relation yields the RDF as

$$f(r) = \frac{1}{\rho \cdot 4\pi r^2} \frac{dn(r)}{dr}. \tag{4}$$

Numerically, Eq. (4) can be evaluated by converting the differential relation to a difference relation so that dn and dr can be approximated as Δn and Δr, respectively.

In the analyses of this paper, $\Delta n(r)$represents the number of digital pixels at a distance between r and $r + \Delta r$ from a given pixel having temperature rises above ΔT_{thres} (see, Fig. 3). Since the RDF is a probability distribution function, the area under the curve is unity, i.e.,

$$\int_{r=0}^{r=\infty} f(r)dr = 1. \tag{5}$$

The radial distribution function profiles computed for the idealized hotspot distribution in Fig. 2 for $\Delta T_{thres} = 10$, 20, 30, and 40 K are shown in Fig. 4. At $r = 0$, $f(r)$ has a finite value. As r increases, $f(r)$ increases and then decreases. The value of r at which $f(r)$ first becomes zero corresponds to the maximum size (MS) of hotspots for a given ΔT_{thres} [see, Fig. 4(b)]. As r further increases, two more peaks are observed, the first at $r = 1$mm and second at 1.41 mm. These peaks correspond to the average nearest neighbor distance (NND) between the hotspots and the average second nearest neighbor distance, respectively. Note that the peaks become higher as the hotspot size decreases due to the normalization of the curves.

When different values for the temperature threshold are used, the distributions of the shapes and sizes of hotspots with temperature increases above the threshold can be characterized. Hotspot sizes are characterized using two different methods. In the first method, the hotspot size is calculated as the diameter of a circle with the same area as the hotspot in 2D. This method is called the equivalent diameter (ED) scheme. To capture the effect of the shape of the hotspots, a second method is also used. In this method, the hotspot size is calculated as the length of the largest line that can be fitted inside the hotspot. This method is called the MS scheme. Together,

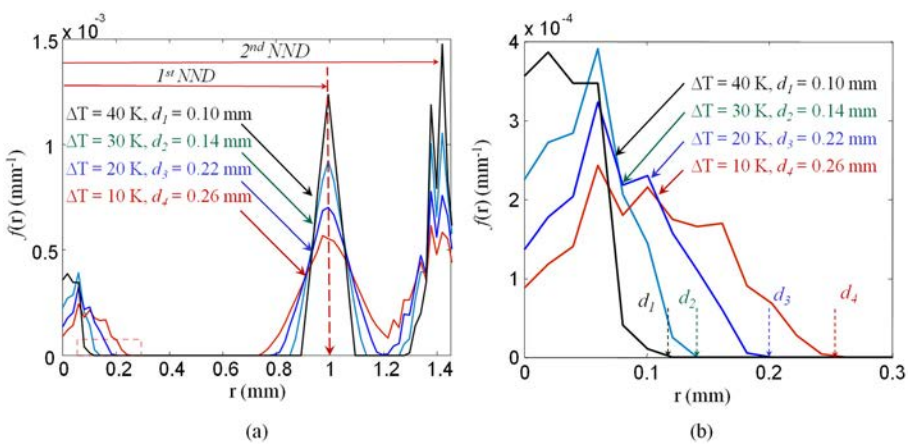

FIG. 4. (a) RDF of the idealized hotspot distribution in Fig. 2 at different cutoff temperatures, and (b) a close-up view of the region where the RDFs go to zero, which shows the diameter of the hotspots at the corresponding cutoff temperatures.

the ED and MS schemes allow quantification of both the size and the shape of hotspots. Systematic characterizations of hotspots are presented in Secs. IV B–IV E.

D. Thermal criticality of hotspots

In the analysis of this paper, critical hotspots are identified using the threshold condition in Eq. (1). The right-hand side of the equation uses Tarver *et al.*'s numerical data (shown in Fig. 1).

The left-hand side of Eq. (1) is obtained by analyzing the hotspot distributions from the CFEM calculations. To account for the variation of temperature within a hotspot (note that temperatures at different spatial locations within a hotspot are different and ΔT_{thres} is the lowest temperature at the periphery), Tarver *et al.*'s criterion is stated as a band of $\pm$ 10% about the mean value. Any hotspot is considered to be critical when it crosses the lower threshold limit (90% of the average threshold). Taking into consideration the stochastic nature of arbitrary microstructures, we employ an approach to identify the time to criticality t_c measured from the onset of dynamic loading. Specifically, instead of one single hotspot, criticality is regarded as being reached if the critical hotspot density in a specimen reaches a level equal to or greater than 0.22 mm^{-2}. This level corresponds to 2 critical hotspots in a 3 mm square domain. It is important to point out that variations in the choice of this parameter do not significantly change the results. Specifically, for a change of critical hotspot density from 0.11 to 0.44 mm^{-2}, the maximum variation in t_c is within 6% for a PBX microstructure having a packing density of 0.82 in several calculations with impact velocities between $v = 50$ and 250 ms^{-1}. This shows that the value of the critical hotspot density chosen is quite reasonable and does not cause large changes in results. Although this treatment contains a degree of arbitrariness, it allows relative comparisons to be made when used consistently for difference cases.

It should be pointed out that calculations are carried out using mesh sizes from 10–20 μm. The results converge as the mesh size is decreased beyond 15 μm. Specifically, the variation of hotspot size leads to a variation of time to criticality t_c of less than 5.0% for a 33% reduction in the mesh size from 15 to 10 μm, suggesting that the mesh resolution chosen (15 μm) is adequate for the purpose of the current study.

In experiments, there is a degree of stochasticity associated with the thermal runaway of hotspots in that quantities such as load intensity required to cause ignition, time to ignition from onset of loading, and total energy input at ignition may vary from sample to sample. One source of the stochasticity is variations in material microstructure and loading conditions. The issue of impact-induced ignition needs to be approached from a probabilistic viewpoint (see, e.g., Ref. 44). Such studies may involve a statistical study using various levels of critical hotspot density and correlation of the results with experimental data.

The time since the onset of dynamic loading at which criticality is reached is taken as the critical time (t_c) and the energy imparted to the specimen per unit load contact area up to this time is taken as the critical input energy density (E).

III. MATERIALS

A. Materials considered

This paper focuses on both granular HMX (GXs) and PBXs, which have two-phase microstructures consisting of HMX grains and an Estane binder. Both idealized and actual microstructures are used to obtain samples with systematically varying attributes. The actual microstructure is obtained from Ref. 45 and has a grain volume fraction of 0.82. It is used to model the PBX, as shown in Fig. 5(a). Additionally, a set of five idealized microstructures are used to model granular HMX. These samples are generated using monomodal and bimodal size distributions of circular grains [representative micrographs are shown in Figs. 5(b)–5(f)]. For this set of five microstructures, two grain sizes are used, with the smaller being 120 μm and the larger being 360 μm. The microstructures analyzed, along with their attributes are listed in Table I. For each attribute listed in Table I, three statistically identical microstructure samples (random instantiations) are generated and used to obtain an estimate of the statistical variation in behavior. The results from the three samples are used in determine the error bounds presented hereafter.

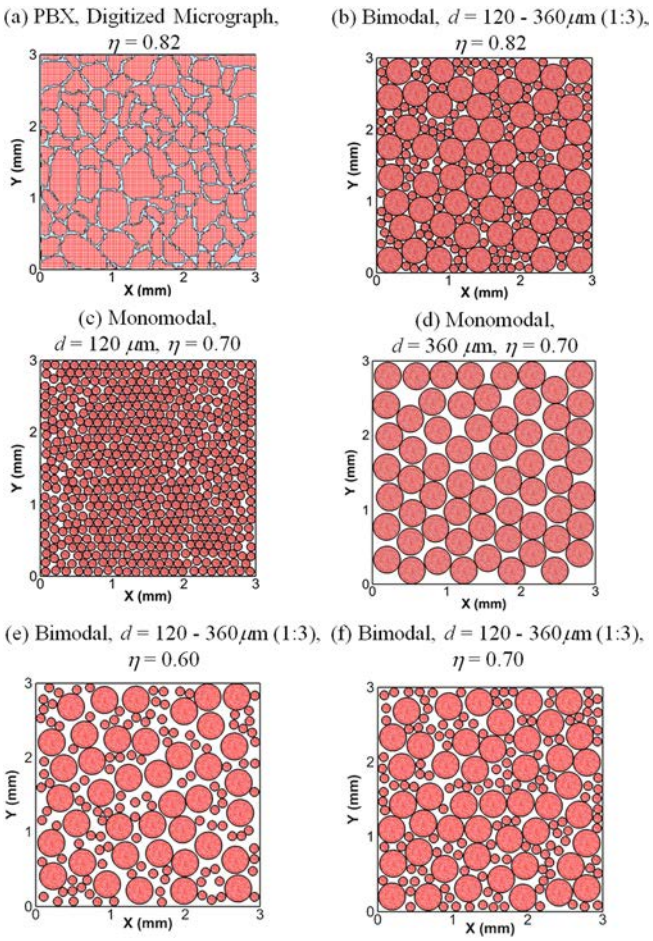

FIG. 5. Microstructures analyzed—digitized image of a PBX and idealized microstructures for granular HMX with different grain size distributions, (a) digitized image of a PBX, (b) bimodal GX, $d = 120$–$360\,\mu$m and $\eta = 0.82$, (c) monomodal GX, $d = 120\,\mu$m and $\eta = 0.70$, (d) monomodal GX, $d = 360\,\mu$m, $\eta = 0.70$ (e) bimodal GX, $d = 120$–$360\,\mu$m and $\eta = 0.60$, and (f) bimodal GX, $d = 120$–$360\,\mu$m and $\eta = 0.70$.

TABLE I. Microstructures analyzed.

Microstructure	Grain volume fraction (η)	Average grain Size (μm)	Attributes
GX (15 instantiations)	0.60	120–360 (1:3)	Bimodal
	0.70	120–360 (1:3)	Bimodal, mono-modal
	0.82	120–360 (1:3)	Bimodal
PBX (Digitized)	0.82	287.4	Real

B. Loading configurations

Calculations are performed using two different loading configurations.

The first is a 3-mm square microstructural region shown in Fig. 6(a). The size of the sample is chosen to

(1) obtain a sufficiently large representative sample of the microstructures—note that this sample size is at least one order of magnitude larger than the length scale of the mean grain size for this type of PBX, giving reasonable representation of the microstructures; and
(2) allow nominally homogeneous states of stress to be reached through stress wave reverberation over the duration of the calculations. This configuration simulates the conditions of split Hopkinson pressure bar experiments.

The specimen is initially stress-free and at rest. The loading configuration is designed to simulate the conditions of nominally uniaxial strain, therefore, the lateral (left and right) boundaries are fixed. The velocity boundary condition at the top surface and the fixed displacement boundary condition at the bottom surface allow prescribed overall deformation rates to be imposed. Loading is effected by applying a constant normal velocity on the top of the sample. The strain-rate $\dot{\varepsilon}$ is calculated by dividing the velocity of the top surface v by the initial height of the specimen. This is a 2D model and the conditions of plane-strain prevail. Since the bottom surface is fixed, this configuration considers the effect of stress wave reflection. For a typical calculation for the PBX, the wave reaches the bottom surface at $\sim$1.15 μs. This can be considered as a delay time before the stress distribution becomes nominally uniform in the sample.

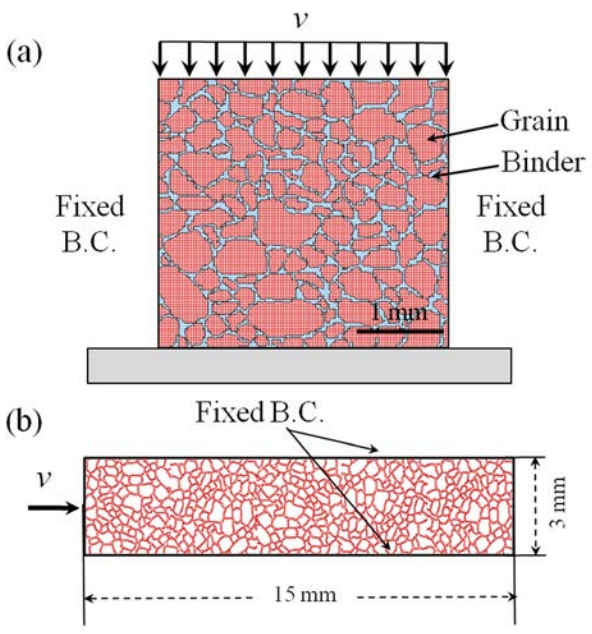

FIG. 6. Loading configurations analyzed, (a) smaller (3 mm × 3 mm) specimen and (b) long specimen with aspect ratio of 5:1 (15 mm × 3 mm).

The second loading configuration involves a 15 mm × 3 mm rectangular microstructural region. This configuration is shown in Fig. 6(b). The upper and lower boundaries are constrained such that lateral expansion (up for the upper edge and down for the lower edge) does not occur. This configuration approximates the normal impact loading of an infinitely wide material block under conditions of macroscopic uniaxial strain. The imposed constant boundary/piston velocity approximately simulates loading under a constant input stress level. The specimen length is chosen to allow approximately the first 5.5-8.5 μs of the propagation of the stress wave from the left surface toward the right to be analyzed, before the wave arrives at the right end.

An important quantity for analyzing the effect of specimen length is the ratio between the domain size in the loading direction and the effective thickness of the steady stress wave. For very small specimens (the ratio being less than unity), the loading configuration allows the effects of high strain rates and full stress wave reflection being analyzed. The loading configuration in Fig. 6(a) is designed with this type of conditions in mind. On the other hand, for the second loading configuration [Fig. 6(b)], the ratio is much larger than unity. That configuration allows the response under conditions of transient stress waves to be analyzed. Naturally, this effect is also dependent on the speed of sound through the specimen and the boundary velocity.

IV. RESULTS AND DISCUSSIONS

The calculations focus on the effects of (i) strain rate, (ii) grain volume fraction ($\eta = 0.60 - 0.82$), and (iii) grain size distribution (monomodal and bimodal). For all calculations presented, the initial temperature is $T_i = 300$ K. The imposed boundary velocity v is varied between 50 and 350 ms^{-1}, yielding overall strain rates of $\dot{\varepsilon} = (16.7 - 116.7) \times 10^3$ s^{-1} [for the loading configuration in Fig. 6(a)]. Since the configuration in Fig. 6(b) focuses on the transient response of microstructures, the relevant discussions are limited to times before the stress wave reaches the boundary on the right [Fig. 6(b)].

A. Hotspot fields

Dissipation associated with mechanisms operative at the grain-level causes localization of thermal energy or the

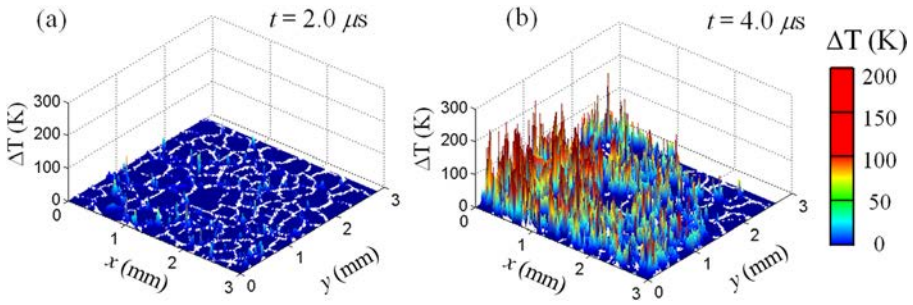

FIG. 7. Evolution of temperature field in the HMX granules of the PBX in Fig. 5(a), ($\eta = 0.82$, $v = 100\,\mathrm{ms}^{-1}$, and $\dot{\varepsilon} = 33.3 \times 10^3\,\mathrm{s}^{-1}$).

formation of hotspots.[26] The evolution of the size, shape, and distribution of hotspots vary significantly with the microstructure and loading. Significant variations in boundary conditions and sample configurations can be encountered during loading. In this section, we discuss a set of calculations on the PBX and GX to quantify the effects on hotspot fields of binder and stress wave reflection.

1. Small samples with wave reflections

Figures 7 and 8 show, respectively, the evolution of hotspots in the grains and binder for a PBX with $\eta = 0.82$ at $t = 2 - 4\,\mu\mathrm{s}$. The impact velocity is $v = 100\,\mathrm{ms}^{-1}$. The calculation is performed using loading configuration 1. Initially at $t = 2\,\mu\mathrm{s}$, hotspots are few and form in locations of stress concentration due to grain-grain interactions. At higher levels of overall deformation [Fig. 7(c)], high temperatures occur at locations of grain-grain interaction and along cracks within the grains, with the latter being a more significant heating mechanism. At $t = 4\,\mu\mathrm{s}$, transgranular fracture of grains result in high temperature rises on the order of 200–300 K in the grains [see, Fig. 7(b)]. Although there is frictional dissipation due to sliding at grain/binder interfaces, the temperature rises in the binder is consistently lower than that in the grains [see, Fig. 8(b)]. In Figs. 7(a) and 7(b), the temperature increases near the lower boundary are higher, due to the fact that the lower boundary is rigid and causes full reflection of the incident stress wave back into the material. This reflection subjects the lower portion of the material to slightly more intense loading.

The temperature rise in the GX having $\eta = 0.82$ at $t = 2 - 4\,\mu\mathrm{s}$ is shown in Fig. 9. The impact velocity is again $v = 100\,\mathrm{ms}^{-1}$. Compared with that in the PBX, the temperature rise during the first 1–2 $\mu\mathrm{s}$ is lower in the GX, since most of the deformation is accommodated by the rearrangement of the grains and elastic intergranular interactions. However, at higher levels of overall deformation $(t = 4\,\mu\mathrm{s})$, fracture of grains and frictional dissipation lead to significantly higher temperature increases throughout the microstructure. The temperature rise is approximately homogeneous in the domain, since the stress wave equilibrates over time (due to multiple reflections from the top and bottom boundaries).

Crushing of the smaller grains typically result in multiple fragments, increasing the surface area available for frictional dissipation. Thus, higher temperature rises are primarily seen at locations where smaller grains are fragmented, whereas the fracture of larger grains generally results in fewer fragments. Consequently, the locations of the higher temperature increases are interspaced by the larger grains [Fig. 9(b)]. A more systematic study of the effect of grain size on the spatial distribution of hotspots is presented in Sec. IV C. At higher levels of overall deformation, transgranular fracture occurs in both smaller and larger grains.

2. Large samples without wave reflections

The next set of calculations illustrates the effect of stress wave propagation in long microstructures [loading configuration 2, Fig. 6(b)]. Figure 10 shows the distributions of temperature in a PBX microstructure with a packing density of $\eta = 0.82$ at $t = 5.2\,\mu\mathrm{s}$. The impact velocity is $v = 100\,\mathrm{ms}^{-1}$. The profile of the average axial stress over the cross section of the specimen is also shown in Fig. 10(a). Note that the sample is long so wave reflection does not occur for the duration analyzed. The time shown here is later than those in the previous figures for the small samples for which wave reflection occurs. The average value of the axial stress behind the wave front is ~361.3 MPa. For higher volume fractions, the average stress can be obtained by extrapolating the value obtained from the CFEM calculations here using Eq. (4.1) in Ref. 46. For a grain volume fraction of 0.95, such as that used in PBX9501, the average stress is predicted to be ~457 MPa, which is within 3.3% of the value obtained from experiments.[47]

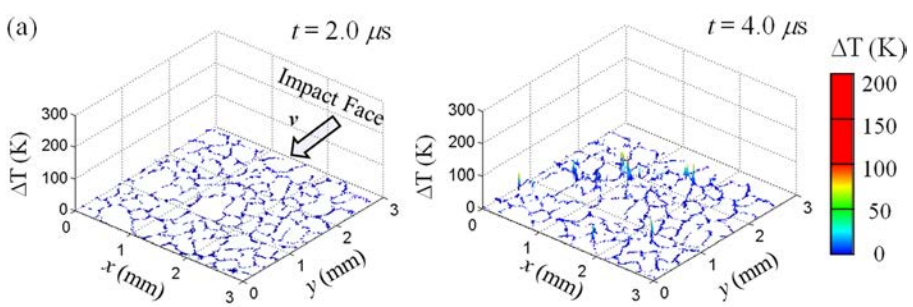

FIG. 8. Evolution of the temperature field in the binder of the PBX in Fig. 5(a), ($\eta = 0.82$ and $v = 100\,\mathrm{ms}^{-1}$, and $\dot{\varepsilon} = 33.3 \times 10^3\,\mathrm{s}^{-1}$).

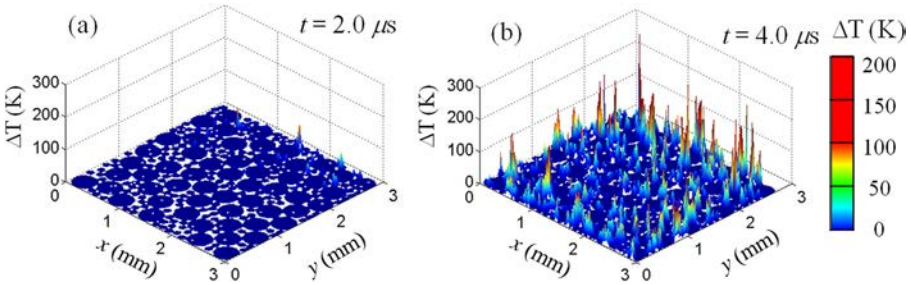

FIG. 9. Evolution of the temperature field in the GX in Fig. 5(b), ($\eta = 0.82$, $v = 100\,\mathrm{ms}^{-1}$, and $\dot{\varepsilon} = 33.3 \times 10^3\,\mathrm{s}^{-1}$).

The temperature increases are highest near the impact surface and gradually decrease away from it. This is a consequence of the stress wave continuing to propagate towards the unstressed material. For this impact velocity, the failure mechanisms (transgranular fracture and sliding frictional heating along crack faces, intergranular interaction, and heating due to binder deformation and crack face friction) occur much behind the initial stress wave front. This results in severe temperature rises of the order of 300–400 K in the grains. High temperature rises also occur in the binder phase, but are lower than those in the grains.

The dominant mechanism responsible for hotpot formation under the conditions analyzed is frictional dissipation as a result of grain fracture. In Ref. 46, the authors quantified the evolution of fracture energy. An analysis of the spatial distribution of fracture energy showed that the maximum fracture dissipation occurs near the impact face and gradually decreases to zero at the front of the stress wave. This causes the highest temperature increases to occur near the impact face as seen in Fig. 10.

Figures 11(a) and 11(b) shows the distribution of temperature in a long GX sample with a packing density of $\eta = 0.82$ at $t = 4.0 - 6.0\,\mu s$. The impact velocity is $v = 100\,\mathrm{ms}^{-1}$. Similar to those in the PBX, the temperature rises are highest near the impact surface. However, due to the absence of any binder, more intergranular interactions occur, resulting in significantly higher hotspot density (number of hotspots per unit area). Quantifications of the hotspot distributions are presented in Secs. IV B and IV C.

The responses of the short [loading configuration 1, Fig. 6(a)] and long samples [loading configuration 2, Fig. 6(b)] are significantly different. For both GX and PBX, the shorter samples experience more uniform temperature rises as a result of multiple stress wave reflections. On the other hand, in the longer samples, the temperature decreases with distance from the loading surface. The overall more uniform hotspot distributions in the smaller samples can be more directly correlated to the initial microstructure and loading conditions. In subsequent discussions on characterizations of the temperature fields and size distributions of the hotspots, the focus is primarily on calculations using loading configuration 1.

B. RDF and hotspot size distributions

The temperature field at any given time has local peaks or hotspots. The individual hotspots can be extracted from the continuous temperature fields using the threshold scheme discussed in Sec. II C. To illustrate this scheme, Figs. 12(a)–12(c) show the hotspot distribution in a PBX microstructure with a packing density of $\eta = 0.82$ at $t = 3.6\,\mu s$. The impact velocity is $v = 100\,\mathrm{ms}^{-1}$. The hotspot fields in Figs. 12(a)–12(c) are obtained using three temperature thresholds of $\Delta T_{thres} = 40$, 200, and 400 K, respectively. At a low threshold of $\Delta T_{thres} = 40$ K, the hotspots are in the form of bands [Fig. 12(a)]. At the higher ΔT_{thres} values, the hotspots become more distinct and sparse. At a high threshold of $\Delta T_{thres} = 400$ K, only two hotspots remain [Fig. 12(c)]. The images clearly show that while hotspot development is extensive throughout the microstructure, only a relatively small number of hotspots have the highest temperatures. It is these highest temperature hotspots that control the ignition process. Since the occurrence of these dominant hotspots is stochastic, it is important to account for the statistical nature of the ignition process resulting from it. The treatment using a critical hotspot density in Sec. II D reflects this consideration. Although simple, it represents a step in the right direction. Further development should certainly be considered in the future.

The RDFs corresponding to the hotspot distributions in Figs. 12(a)–12(c) are shown in Figs. 12(d)–12(f). At $\Delta T_{thres} = 40$ K, the RDF is continuous and does not indicate any distinct hotspots. This indicates that most of the hotspots are still connected [see Fig. 12(a)]. At a threshold of $\Delta T_{thres} = 200$ K, the RDF profile first reaches zero at $r \sim 0.3$ mm, which is the diameter of the largest hotspot. The next peak of the RDF occurs around $r = 0.6$ mm. This is the

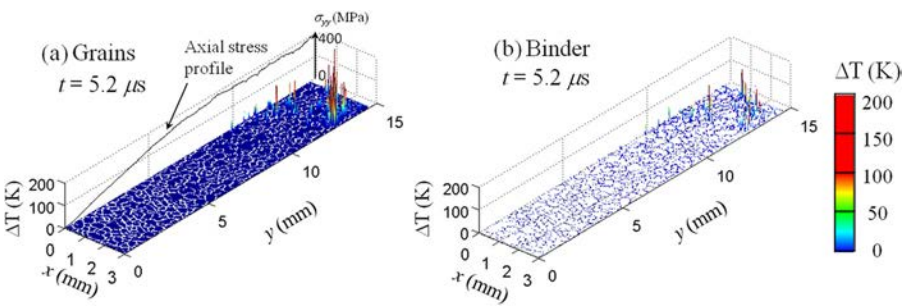

FIG. 10. Temperature field in the grains and binder for loading configuration 2 (PBX in Fig. 5(a), $\eta = 0.82$ and $v = 100\,\mathrm{ms}^{-1}$).

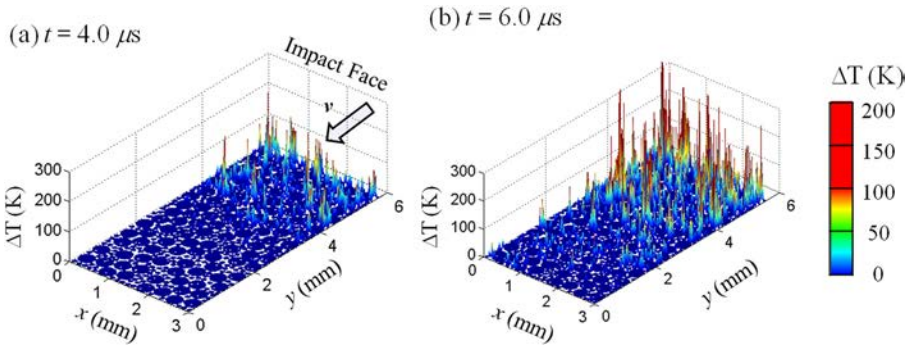

FIG. 11. Evolution of the temperature field in HMX for loading configuration 2 (GX in Fig. 5(b), $\eta = 0.82$ and $v = 100\,\mathrm{ms}^{-1}$).

average spacing between the first near neighboring hotspots. Finally, at $\Delta T_{thres} = 400\,\mathrm{K}$, there are only two hotspots remaining [see, Fig. 12(c)] and the RDF [Fig. 12(f)] clearly shows the size of the largest hotspot and the distance between the two.

The morphologies of hotspots are distinct and varied. This can influence the ignition threshold and subsequent burn. Previous studies[1,7] have analyzed the effect of hotspot shapes on the ignition threshold and the time to ignition. Specifically, Tarver *et al.*[1] analyzed hotspots of three different geometries and found that the critical temperature was not significantly affected by the hotspot shape. However, in a microstructural setting, the shape of the hotspots may significantly influence the connectivity of neighboring hotspots. For example, elongated hotspots may result in the formation of high temperature bands [Fig. 12(a)]. This can significantly affect the propagation of reaction subsequent to ignition.

To quantify the variation of hotspot shapes, the ED and MS schemes are used to determine the hotspot distributions for the calculations shown in Fig. 12. Figures 13(a)–13(c) show the size distributions obtained using the ED scheme, and Figs. 13(d)–13(f) show the corresponding size distributions using the MS scheme. Clearly, a higher density of larger-size hotspots is detected using the MS scheme. As an example of the difference in results, at a threshold of $\Delta T_{thres} = 200\,\mathrm{K}$, the maximum hotspot size using the ED scheme is $\sim$0.1 mm while that obtained using the MS scheme is $\sim$0.2 mm. The size of the largest hotspot predicted by the RDF [Figs. 12(d)–12(f)] is almost identical to hotspot sizes obtained using the MS scheme [Figs. 13(d)–13(f)]. However, it is noted that the overall density of the hotspots are similar in both cases. In the subsequent analysis, the MS scheme is used to quantify the size of hotspots, since it provides the largest dimensions of the hotspots and can be correlated more readily with information from the RDFs.

C. Effect of initial porosity

Porosity is present in all GXs and has a significant influence on their impact sensitivities.[48,49] In applications, it is desirable to have lower porosity for higher energy output. The effect of porosity is analyzed by deforming three GX

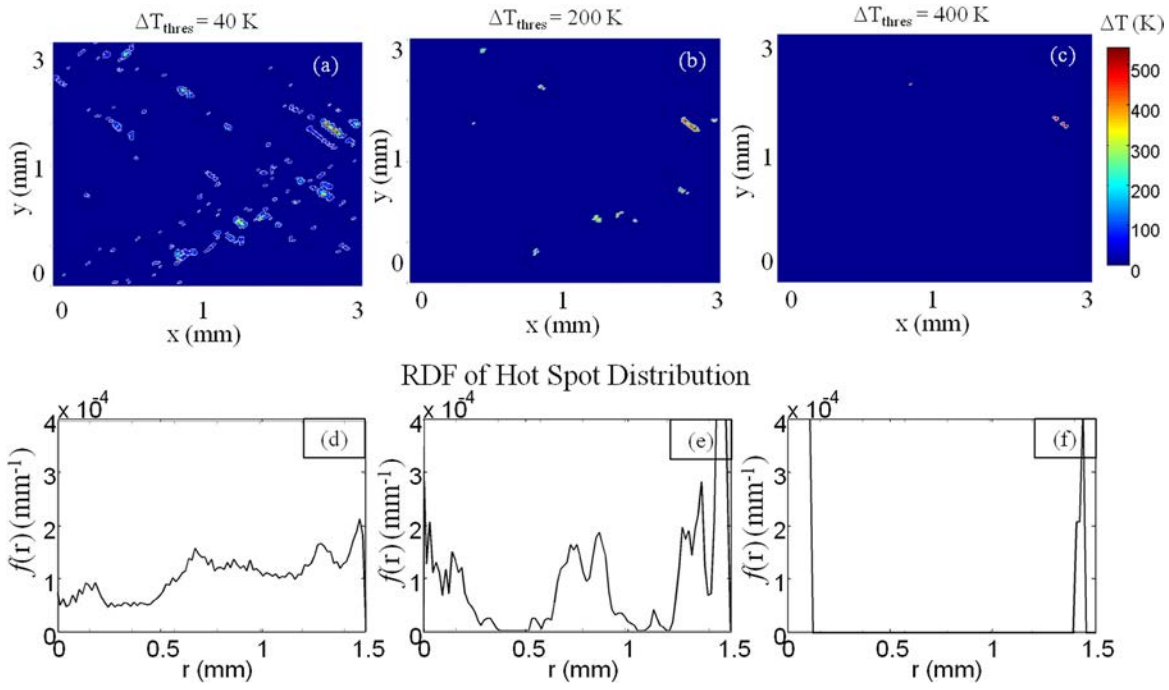

FIG. 12. Distribution of hotspots obtained using different temperature thresholds (a) 40 K, (b) 200 K, and (c) 400 K and the corresponding RDFs at (d) 40 K, (e) 200 K, and (f) 400 K (PBX, $\eta = 0.82$, $v = 100\,\mathrm{ms}^{-1}$ and $\dot{\varepsilon} = 33.3 \times 10^3\,\mathrm{s}^{-1}$).

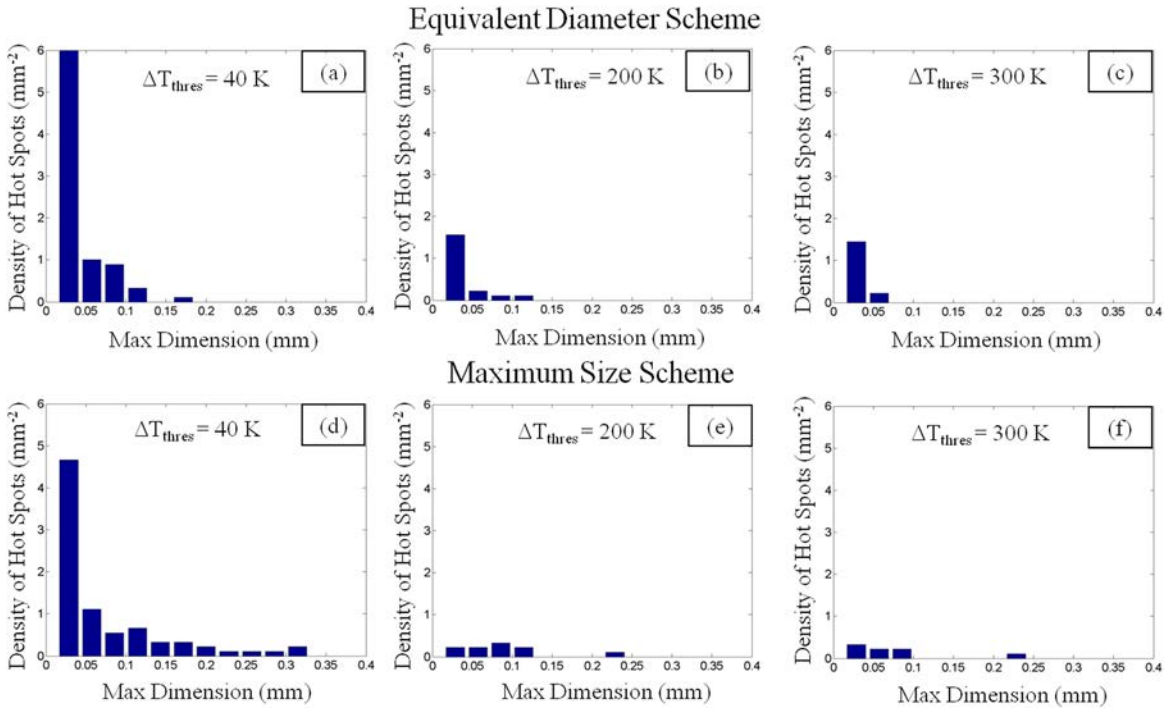

FIG. 13. Size distributions of hotspot in HMX granules obtained using the diameter of a circle of equal area for different temperature thresholds (a) 40 K, (b) 200 K, and (c) 400 K, and using the maximum dimension for different temperature thresholds (d) 50 K, (e) 200 K, and (f) 400 K (PBX, $\eta = 0.82$, $v = 100\,\mathrm{ms}^{-1}$, and $\dot{\varepsilon} = 33.3 \times 10^3\,\mathrm{s}^{-1}$).

microstructures having initial volume fractions of $\eta = 0.60$, 0.70, and 0.82 [Figs. 5(b), 15(e), and 15(f)], respectively. Figures 14(a)–14(c) show the distribution of temperature at $t = 5.4\,\mu\mathrm{s}$. The impact velocity is $v = 100\,\mathrm{ms}^{-1}$. The calculations are performed using loading configuration 1 [Fig. 6(a)]. Clearly, the temperature increases with η for the same value of overall strain. For $\eta = 0.60$, the temperature increases are low and only occurs at locations of grain-grain interactions. Higher volume fractions decrease the initial porosity, thereby enhancing grains-grain interactions and transgranular fracture. The overall effective wave speed also increases with the volume fraction. Consequently, under the same impact velocity, microstructures having higher grain volume fractions experience high temperature increases over a larger domain.

The distributions of hotspots are distinct for each value of porosity. To analyze the effect of initial porosity, Figs. 15(a)–15(c) show the RDFs and Figs. 15(d)–15(f) show the size distributions for the three calculations with initial volume fractions of $\eta = 0.60$, 0.70, and 0.82 at $t = 10.8$, 7.6, and $5.2\,\mu\mathrm{s}$, respectively. The time at which the RDFs and size distributions are obtained correspond to the critical time for ignition (to be discussed in more detail later) t_c for each of the microstructures at an impact velocity of $v = 100\,\mathrm{ms}^{-1}$.The RDFs show the formation of distinct hotspots with an average hotspot spacing of ~0.6 mm. The maximum hotspot size and average distance between hotspots show no appreciable variation with the initial volume fraction. This indicates that the initial porosity does affect the spatial distribution of hotspots at t_c. Rather, it is the size and size distribution of the granules that set the scale for the spacing between hotspots for GXs. The hotspot size distributions are also similar for the different porosities analyzed, indicating that the heating is primarily due to fracture and frictional dissipation occurring when the GX is pressed to higher densities. It should be noted that this result is for impact velocities in the range between $v = 50$ and $250\,\mathrm{ms}^{-1}$ and may not be applicable to scenarios with much higher

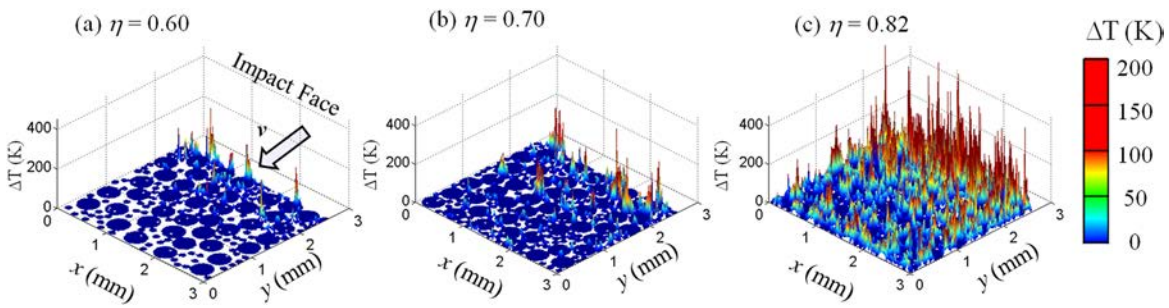

FIG. 14. Distribution of hotspots in GX with different initial volume fractions: (a) $\eta = 0.60$, (b) $\eta = 0.70$, and (c) $\eta = 0.82$, (Bimodal GX, $d = 120$–$360\,\mu\mathrm{m}$, $v = 100\,\mathrm{ms}^{-1}$, $\dot{\varepsilon} = 33.3 \times 10^3\,\mathrm{s}^{-1}$, and $t = 5.4\,\mu\mathrm{s}$).

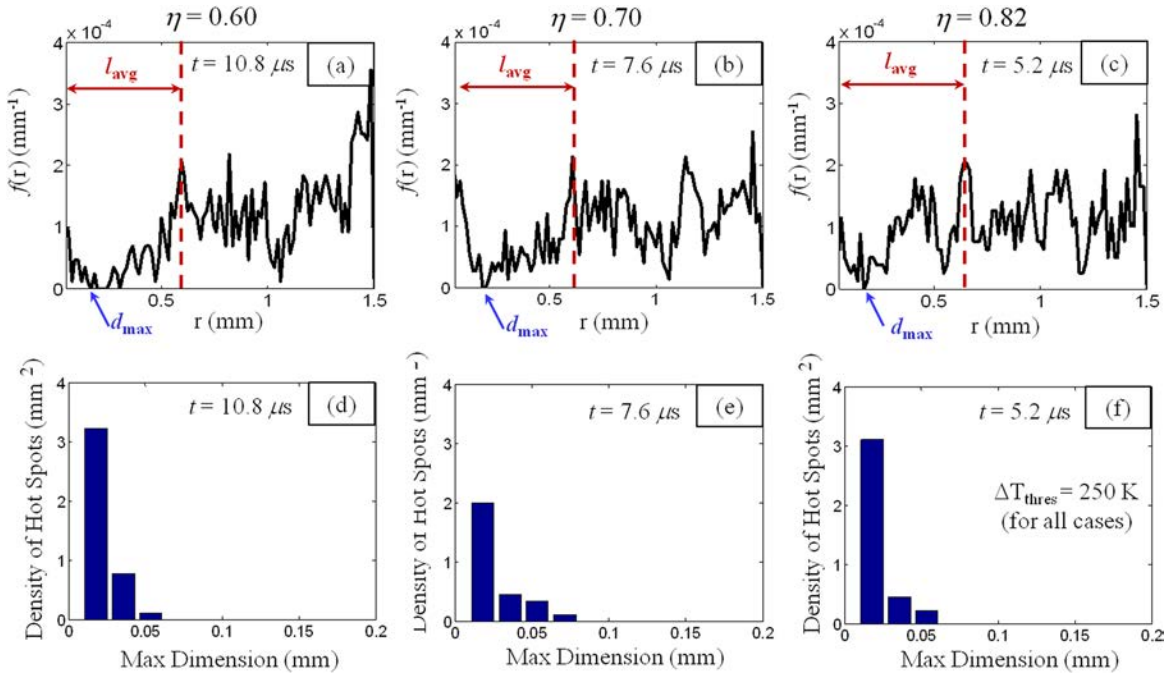

FIG. 15. RDFs of the temperature field in microstructures of GX having different initial porosity levels (a) $\eta = 0.60$, (b) $\eta = 0.70$, and (c) $\eta = 0.82$, and ((d)–(f)) the corresponding hotspot size distributions obtained using the maximum dimension method (bimodal distribution GX, $v = 100\,\mathrm{ms}^{-1}$ and $\dot{\varepsilon} = 33.3 \times 10^3\,\mathrm{s}^{-1}$).

impact velocities (e.g., during shock loading) where additional dissipation mechanisms (such as void collapse, jetting, etc) may influence the formation of hotspots.

D. Effect of impact velocity

The effect of loading rate is analyzed by deforming the PBX microstructure in Fig. 5(a), and the GX microstructure in Fig. 5(b) at the two impact velocities of $v = 50$ and $250\,\mathrm{ms}^{-1}$. The corresponding strain rates are the range of $\dot{\varepsilon} = (16.7 - 116.7) \times 10^3\mathrm{s}^{-1}$. The calculations are performed on the PBX and GX microstructures using loading configuration 1 [Fig. 6(a)]. Figure 16 shows the distributions of temperature at a nominal strain of 10.0%.

At a low impact velocity of $50\,\mathrm{ms}^{-1}$, the temperature increase in the PBX is higher than that in the GX. In the PBX, the binder is softer, allowing the temperature rise to be spread out over the entire microstructure. Additionally, the absence of any porosity in the PBX leads to higher stresses, subsequent fracture, and frictional dissipation. In contrast, in the GX, rearrangement of the grains reduces the stress in the early part of loading. At later stages of loading, fragments

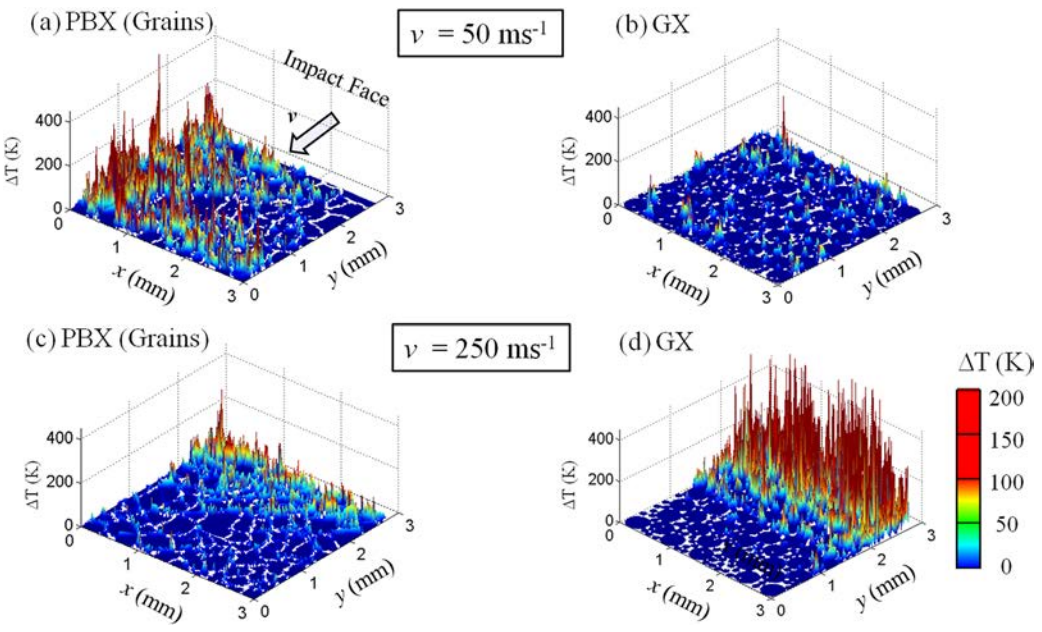

FIG. 16. Distribution of hotspots in HMX at the same nominal strain of $\varepsilon = 10.0\%$, (a) PBX, $v = 50\,\mathrm{ms}^{-1}$, (b) GX, $v = 50\,\mathrm{ms}^{-1}$, (c) PBX, $v = 250\,\mathrm{ms}^{-1}$, and (d) GX, $v = 250\,\mathrm{ms}^{-1}$ [$\eta = 0.82$ and $\dot{\varepsilon} = (16.7\text{–}83.3) \times 10^3\,\mathrm{s}^{-1}$].

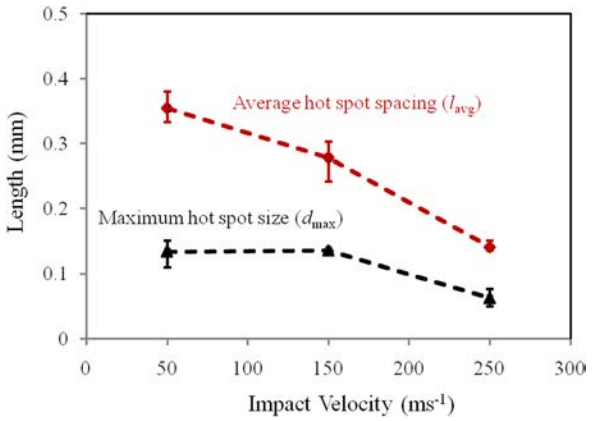

FIG. 17. Effect of impact velocity on the maximum hotspot size and average hotspot spacing ($\eta = 0.82$, bimodal GX, $v = 50$–$250\,\mathrm{ms}^{-1}$, $\dot{\varepsilon} = 16.7$–$83.3 \times 10^3\,\mathrm{s}^{-1}$, and $\Delta T_{thres} = 100$–$570\,\mathrm{K}$).

generated from grain fracture occupy the vacant areas (pores), resulting in lower overall stresses compared to the PBX. This leads to a lower temperature increase for the GX.

However, at higher impact velocities ($v = 250\,\mathrm{ms}^{-1}$), grain-grain interaction and transgranular fracture become the primary dissipation mechanisms even at early stages of loading. For both PBX and GX [Figs. 16(c) and 16(d)], the distribution of hotspots is concentrated near the impact face where the most severe temperature increases occur. The temperature increase in the GX is higher than that in the PBX (in contrast to the behavior seen at the lower impact velocity). For the PBX, deformation of the binder reduces the stress level and prevents grain-grain interactions in the early part of loading. On the other hand, the GX experiences grain-grain interactions and transgranular fracture immediately upon impact, which results in high temperature increases. Thus, for the conditions analyzed, the GX appears to be less sensitive at low impact velocities, whereas the PBX is less sensitive at higher impact velocities.

The effect of loading rate on the maximum hotspot size (d_{max}) and average hotspot spacing (l_{avg}) is shown in Figure 17 for a GX with $\eta = 0.82$ at a nominal strain of 10.0%. The impact velocity is varied between $v = 50$ and $250\,\mathrm{ms}^{-1}$. The results show that d_{max} does not change significantly over $v = 50 - 150\,\mathrm{ms}^{-1}$. However, as the impact velocity increases beyond $v = 150\,\mathrm{ms}^{-1}$, d_{max} starts to decrease. This suggests that the hotspots tend to become more localized at higher loading rates. As v increases, the average hotspot spacing l_{avg} decreases approximately linearly. In the regime of $v = 50 - 250\,\mathrm{ms}^{-1}$, l_{avg} decreases by a factor of 2.5. This is due to earlier fracture and greater fragmentation of the grains at the higher impact velocities, resulting in a higher density of hotspots.

E. Effect of grain size distribution

Several studies have tried to correlate the size,[50] morphology,[51] and surface area[52] of crystalline granules with impact sensitivity. Czerski[51] reported that there was no clear correlation between size and the sensitivities of small ($\sim 10\,\mu$m) and medium ($\sim 100\,\mu$m) sized 1,3,5-Trinitroperhydro-1,3,5-triazine particles. Lecume[53] suggested that the surface roughness may affect impact sensitivity. The sensitivity of GX is also dependent on the strength of loading. Chakravarty[54] found that at low pressure and long duration loading waves, larger grain sizes correspond to higher impact sensitivity.

To illustrate the effect of grain size on hotspot field, three different GX microstructures having the same volume fraction ($\eta = 0.70$) are analyzed: (A) monomodal, $d = 120\,\mu$m, (B) monomodal, $d = 360\,\mu$m, and (C) bimodal, $d = 120$-$360\,\mu$m (henceforth referred to as microstructure A, B and C, respectively). Figures 18(a)–18(c) show the distributions of temperature in the 3 mm square specimens, at $t = 8.0\,\mu$s for an impact velocity of $v = 100\,\mathrm{ms}^{-1}$.The temperature increases at the same amount of nominal strain are quantitatively similar for all cases, indicating that grain size may not have a significant influence on impact sensitivity.

However, the spatial distributions of hotspots are affected by the grain size. Figures 19(a)–19(c) show the RDFs and Figs. 19(d)–19(f) shows the size distributions of hotspots in these microstructures at $t = 8.0\,\mu$s. The RDFs show that the maximum size (0.07–0.17 μm) of hotspots increases only slightly with grain size. On the other hand, the average distance between hotspots is largest for microstructure C (0.53 μm), followed by B (0.18 μm) and A (0.13 μm). The issue relates to the temperature distributions shown in Figs. 18(a)–18(c). In the case of (A), the fragmentation of the small grains ($d = 120\,\mu$m) and subsequent frictional dissipation at the fracture surfaces result in hotspots forming very close to each other. The average distance between hotspots is low and of the order of the maximum size of hotspots ($\sim$0.15–0.2 mm). In the case of (B), which is composed of larger grains ($d = 360\,\mu$m), hotspots primarily form at locations of grain-grain interactions, rather than due to complete

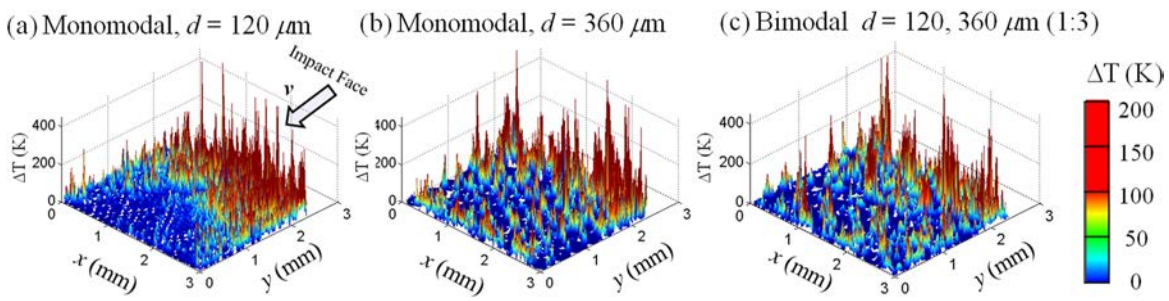

FIG. 18. Distribution of hotspots in GX with different grain size distributions: (a) monomodal, $d = 120\,\mu$m, (b) monomodal, $d = 360\,\mu$m, and (c) bimodal, $d = 120$–$360\,\mu$m ($\eta = 0.70$, $v = 100\,\mathrm{ms}^{-1}$, $\dot{\varepsilon} = 33.3 \times 10^3\,\mathrm{s}^{-1}$, and $t = 8.0\,\mu$s).

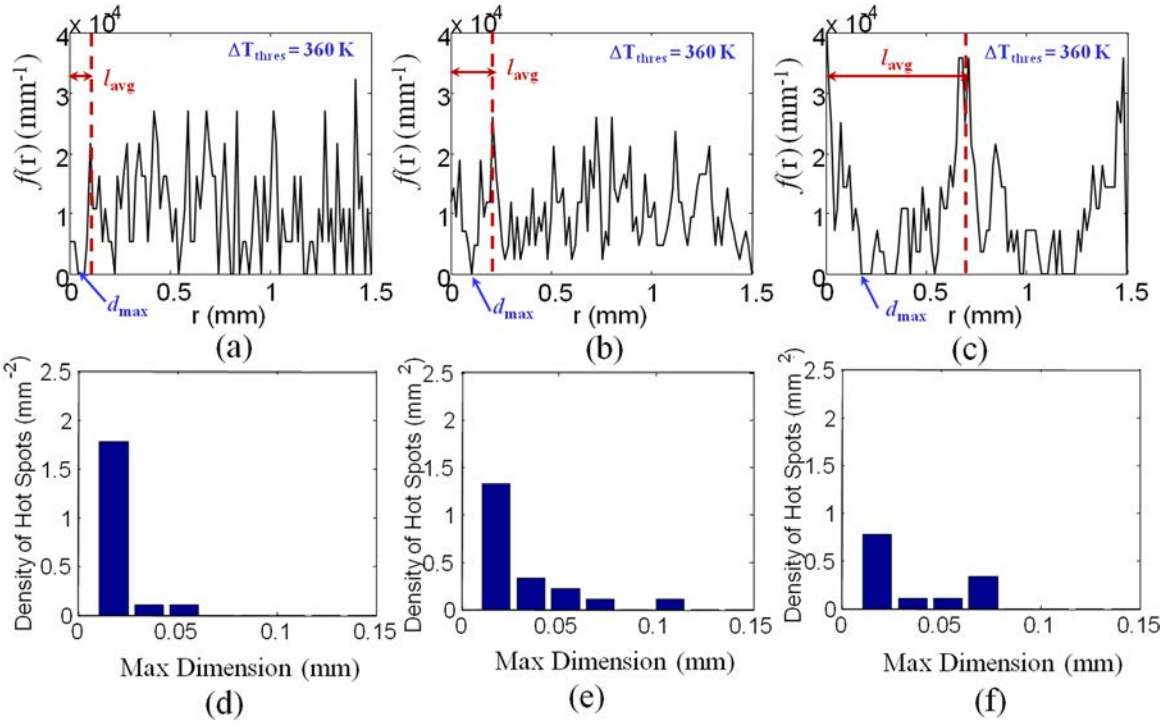

FIG. 19. RDFs of the temperature fields in microstructures of GX having different grain size distributions (a) monomodal, $d = 120\,\mu$m, (b) monomodal, $d = 360\,\mu$m, and (c) bimodal, $d = 120$–$360\,\mu$m, and ((d)–(f)) the corresponding hotspot size distributions obtained using the maximum dimension method ($\eta = 0.70$, $v = 100\,\text{ms}^{-1}$, $\dot{\varepsilon} = 33.3 \times 10^3\,\text{s}^{-1}$, and $t = 8.0\,\mu$s).

crushing of the grains. however, fragmentation of grains results in multiple hotspots forming close to each other, which leads to an average hotspot spacing of ~ 0.25 mm (in comparison, the grain size is 0.36 mm). For (C), which has a bimodal distribution of grains, hotspots arise due to the crushing of the smaller grains. The average spacing between these hotspots (~ 0.6 mm) is consequently influenced by the distribution of the larger grains.

Figure 20 shows the maximum hotspot size (d_{max}) and average hotspot spacing (l_{avg}) for microstructures A, B, and C at $t = 5.4\,\mu$s. The impact velocity is $v = 100\,\text{ms}^{-1}$. Note that for each microstructure, multiple random instantiations are used, yielding the ranges of data shown. Clearly, d_{max} varies only slight among the cases, suggesting that ignition sensitivity is not significantly affected by grain size. On the other hand, l_{avg} increases significantly with grain size, with the bimodal distribution showing higher l_{avg} than both monomodal size distributions. Obviously, the issue is a complex one.

In currently available ignition theories, while the size of hotspots is considered very important, inter-hotspot distance is explicitly not considered. Indeed, it must be noted that the thermal ignition criteria presented in Sec. II does not account for spacing in between hotspots. However, it is generally accepted that the spatial arrangement of hotspots influences the post ignition burn, specifically the deflagration to detonation transition (DDT) phenomena. The systematic quantification that comes out of the RDF analyses here may lead to an examination of this issue in the future. In this paper, only the size and temperature of hotspots are considered.

F. Connecting hotspot statistics to thermal criticality data of Tarver et al.

Hotspot distributions are analyzed using the scheme presented in Sec. II D to identify critical hotspots that may lead to ignition. To illustrate the process of how critical hotspots are identified, Figs. 21(a)–21(d) show the hotspots detected in the grains for a calculation on a PBX specimen with a HMX volume fraction of $\eta = 0.82$. The imposed boundary velocity is $100\,\text{ms}^{-1}$. In general, the sizes and temperatures of hotspots increase with time, as shown by the group of hotspots, which move towards the threshold region for times between $t = 5.2 - 7.2\,\mu$s. The three curves denote Tarver

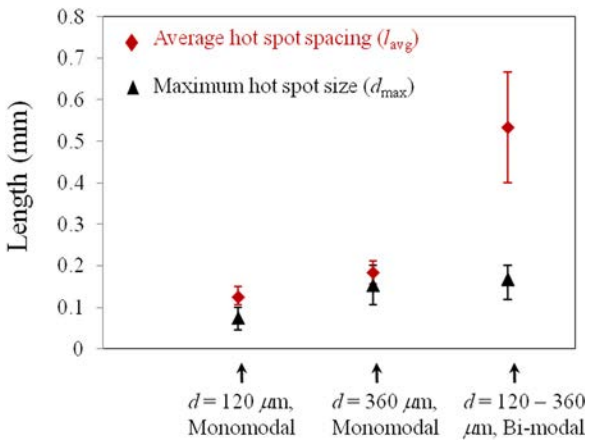

FIG. 20. Effect of grain size on the maximum hotspot size and average hotspot spacing [GX in Figs. 5(c)–5(d) and 5(f)], $\eta = 0.70$, $v = 100\,\text{ms}^{-1}$, and $\dot{\varepsilon} = 33.3 \times 10^3\,\text{s}^{-1}$).

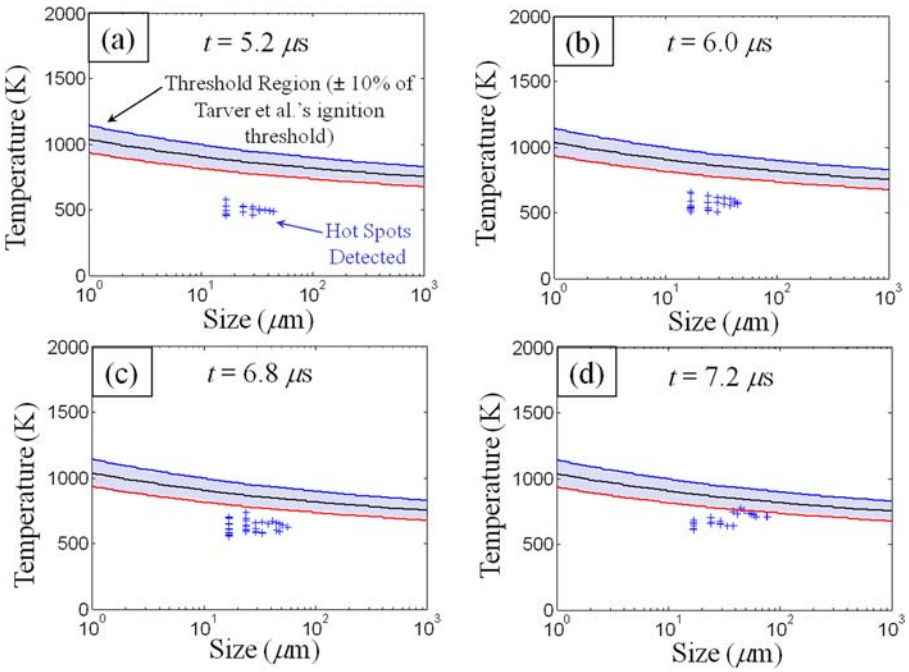

FIG. 21. Size and temperature of hotspots relative to Tarver *et al.*'s ignition threshold at different times between $t = 5.2$–$7.2\,\mu s$ [PBX Fig. 5(a)], $\eta = 0.82$ and $v = 100\,ms^{-1}$).

et al.'s criticality data stated as a band of ± 10% about the mean value, as discussed in Sec. II D. A hotspot is considered to be critical when it crosses the lower threshold limit (90% of the average threshold). The figure shows that the hotspots, up to a time of $t = 6.8\,\mu s$, are below the threshold and not considered critical. At $t = 7.2\,\mu s$, the hotspots having the highest temperatures cross the lower threshold. Once the criterion outlined in Sec. II D is satisfied, the material is assumed to have reached the critical state for thermal runaway. The time (measured from the beginning of loading) at which this is taken as the time to criticality (t_c) and is obtained for different cases of impact velocity, grain volume fraction, and size distribution.

Figure 22(a) shows the variation of critical time t_c with boundary velocity v for PBX and GX microstructures having an initial volume fraction of $\eta = 0.82$ [Figs. 6(a) and 6(b)]. The calculations are performed for a range of impact velocities between $v = 50$ and $250\,ms^{-1}$,using loading configuration 1 [Fig. 6(a)]. The results are fitted to a curve of the form $v^n t = c(\eta)$ to illustrate the overall trends. Here, $c(\eta)$ is a function of initial porosity. In general, for both PBX and GX, as the boundary velocity increases, the time to criticality decreases. This is similar to the shock response of explosives.[2,55,56]

At high impact velocities $(v > 100\,ms^{-1})$, the time to criticality for the PBX is 2–4 times that for the GX. This is supported by the results presented in Sec. IV D. In the case of the PBX, the binder deforms to absorb the loading due to the impact, thereby preventing direct grain-grain interactions and minimize fracture during the initial stages of loading. On the other hand, at lower impact velocities $(v < 100\,ms^{-1})$, the PBX is more sensitive than the GX and has a lower time to criticality. This is due to the higher confinement stresses which arise from the lack of room for compaction, leading to greater fracture and higher temperature rises in the grains. Another aspect of the loading which may contribute to the difference in the sensitivities of PBX and GX is the thickness of the stress wave front. This rise time is smaller for the PBX than for the GX. This difference is more pronounced at lower impact velocities.

For the loading configuration used and over the range of conditions analyzed, t_c continues to decrease as v increases [Fig. 22(a)] and there appears to be a minimum time required for ignition regardless of impact velocity. On the other hand,

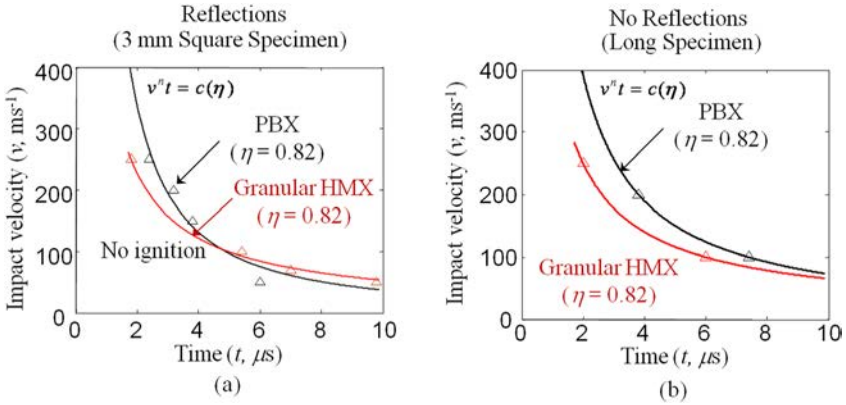

FIG. 22. Time to criticality for PBX and GX using (a) 3 mm square specimen and (b) long specimen ($\eta = 0.82$ and $v = 50$–$250\,ms^{-1}$).

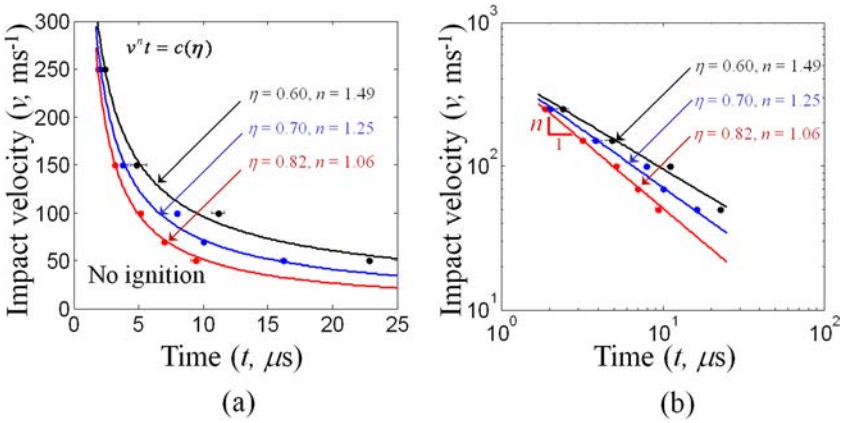

FIG. 23. Time to criticality for GX having a range of initial grain volume fractions $\eta = 0.60$–0.82, plotted using (a) linear scale (b) log-log scale ($\eta = 0.70$–0.82 and $v = 50$–$250\,\mathrm{ms}^{-1}$).

the range of data does not appear to suggest the existence of a low velocity cutoff below which no ignition occurs. One possible explanation is that the successive wave reflections from the top and bottom surfaces [Fig. 6(a)], leads to continuing accumulation of elastic strain energy in the specimen. This accumulation can lead to sudden fracture and frictional dissipation with sustained loading, causing high temperature rises even at low impact velocities.

Figure 22(b) shows the results of calculations having the same initial conditions as those in Fig. 22(a), but for loading configuration 2 [Fig. 6(b)]. Two important differences are clear in the responses of the short and long samples. First, in the calculations using the long specimen [Fig. 6(b)], the PBX is always less sensitive than the GX. However, the difference in sensitivities of the PBX and GX increases with the impact velocity, suggesting that the protective effect of the binder in the PBX is more pronounced under severe loading. Second, for a long specimen, no critical hotspots are obtained at impact velocities lower than $100\,\mathrm{ms}^{-1}$. This indicates the existence of a minimum velocity below which no critical hotspot (and, therefore, no ignition) occurs. The existence of the lower velocity threshold can be explained on the basis of the constant strength of the stress wave behind the initial wave front. Since there is no wave reflection, no significant temperature increase occurs in the grains once the stress wave has passed.

The effect of porosity is analyzed by comparing the criticality response of three GX microstructures having initial volume fractions of $\eta = 0.60$, 0.70, and 0.82 [Figs. 5(b), 5(e), and 5(f)]. Figures 23(a) and 23(b) show the variation of the critical time t_c as a function of the boundary velocity, which is varied between $v = 50$ and $250\,\mathrm{ms}^{-1}$. The calculations are performed using loading configuration 1 [Fig. 6(a)]. Overall, the higher the initial volume fraction η, the more sensitive is the GX. The variation in response with η is small at high impact velocities, with a delay time of $t_c \sim 4\,\mu\mathrm{s}$ for all values of η considered. The similarity in response is due to the fact that at high impact velocities, grain fracture (and fragmentation) occurs almost immediately upon impact, leading to high temperature increases in the grains near the impact surface. However, the sensitivity is significantly different at low impact velocities, with a critical time of $t_c = 23.0$ and $9.0\,\mu\mathrm{s}$, for $\eta = 0.60$ and 0.82, respectively, for impact velocity $v = 50\,\mathrm{ms}^{-1}$.

The effect of grain size on criticality is investigated using microstructures A, B, and C (defined in Sec. IV E). Figures 24(a) and 24(b) show the variation of the critical time, t_c as a function of the boundary velocity, which is varied between $v = 50$ and $250\,\mathrm{ms}^{-1}$. The two plots show the data in both linear and logarithmic scales, allowing the trends and key parameters to be identified easily. The calculations are performed using loading configuration 1 [Fig. 6(a)]. The time to criticality for all three microstructures A, B, and C overlap each other, indicating that the grain size distribution (monomodal, bimodal) does not affect the ignition sensitivity. This is also indicated by the hotspot distribution in the microstructures [see, Figs. 18(a)–18(c)], which shows similar temperature increases for all cases. In all

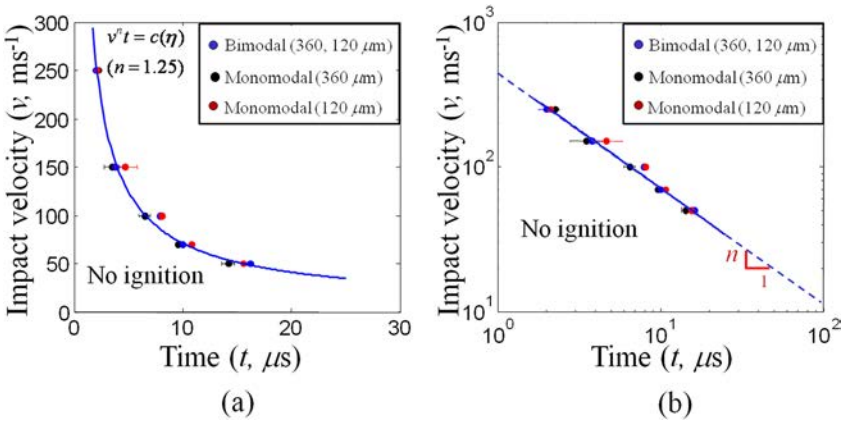

FIG. 24. Time to criticality for GXs having different grain size distributions: monomodal, $d = 120\,\mu\mathrm{m}$, $d = 360\,\mu\mathrm{m}$, and bimodal, $d = 120$–$360\,\mu\mathrm{m}$, plotted using (a) linear scale (b) log-log scale ($\eta = 0.70$ and $v = 50$–$250\,\mathrm{ms}^{-1}$).

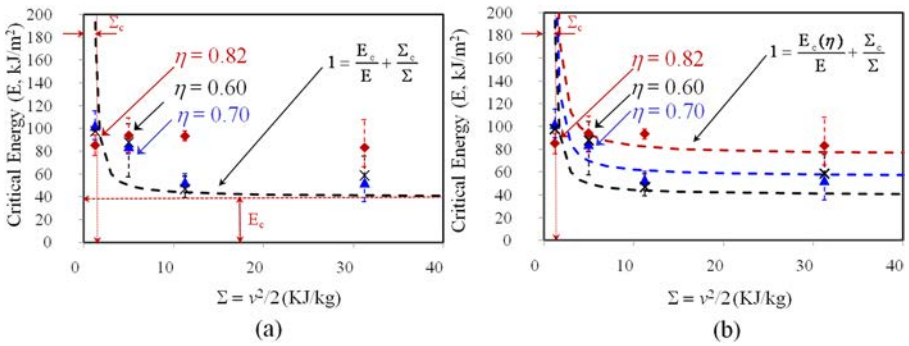

FIG. 25. Critical input energy as a function of Σ for GXs with grain volume fractions between $\eta = 0.60$–0.82, the impact velocities are between $v = 50$–$250\,\mathrm{ms}^{-1}$.

cases, the dominant heating mechanism is sliding friction at grain boundaries and at surfaces generated by grain fracture. It is noted that at higher load intensities including shock loading, there may be additional mechanisms (such as dislocations, phase transformation, and collapse of voids or defects) which may cause the response to be more sensitive to grain size or grain size distribution. Such factors are not considered here.

G. Critical input energy at ignition

One of the measures for assessing the impact sensitivity of an energetic material is the critical input energy E, which is the energy absorbed by or imparted to the material per unit contact area up to the critical time of ignition t_c. Impact resulting in transfer of energy higher than E will lead to detonation.[2,10] Thus, the critical energy lends itself to being used as a parameter in empirical criteria for identifying conditions under which an explosive will ignite. In case of shock, the critical energy is found to be dependent on the shock velocity, shock pressure, and shock duration.[2] However, for impact loading not leading to shock, energy localization is significantly affected by microstructural heterogeneity and grain level failure mechanisms. It is, therefore, important to recognize the difference and quantify the effects properly.

To analyze the effect of initial porosity of GX in this regard, Fig. 25(a) shows the variation of the critical input energy as a function of $\Sigma = (v^2/2)$ for three calculations with GXs having initial volume fractions of $\eta = 0.60$, 0.70, and 0.82 [microstructures in Figs. 5(b), 5(e), and 5(f)]. The impact velocity is varied between $v = 50$ and $250\,\mathrm{ms}^{-1}$. For $\eta = 0.60$ and 0.70, the critical energy absorbed is approximately the same. Overall, E decreases as the impact velocity increases for $\eta = 0.60$ and 0.70, but does not show significant variation with impact velocity for $\eta = 0.82$. For the higher porosities ($\eta = 0.60$ and 0.70), the grains need to be sufficiently compacted before fracture (and, therefore, the frictional dissipation which leads to higher temperatures) initiates. Consequently, at lower impact velocities, higher amounts of energy need to imparted to the specimen to achieve criticality. At higher impact velocities ($v \geq 250\,\mathrm{ms}^{-1}$), fracture occurs earlier, hence critical hotspots are generated at a lower energy threshold. On the other hand, for $\eta = 0.82$, the energy absorbed by the GX is similar at all impact velocities considered. This is likely due to the fact that, at higher volume fractions, intergranular friction, and grain failure occur early. Consequently, most input energy is expended on causing failure. As a result, no significant impact velocity dependence of the critical input energy is seen.

James[2] earlier proposed an energy cutoff E_c within this context for explosives subject to shock loading. The particular form he used to characterize experimental data with this cutoff in mind is

$$1 = \frac{E_c}{E} + \frac{\Sigma_c}{\Sigma}, \tag{6}$$

where E_c is the cutoff input energy below which no ignition occurs and Σ_c is a cutoff velocity (or kinetic energy) measure below which an infinite amount of input energy is required. The reasoning behind the cutoffs in the Hugh James (HJ) relation is that experimental data tend to asymptote towards E_c and Σ_c at very high and very how impact velocities, respectively.[2] Figure 25(a) also shows Eq. (6) (black line) as a fit to the CFEM results for all the cases analyzed. The curve appears to be able to describe the data in the high and low velocity regimes for low volume fraction ($\eta = 0.60$), but considerably under-predicts the response (predicts ignition threshold values lower than the data points) for $\eta = 0.70$–0.82. Obviously, the data suggest a strong influence of microstructure on behavior and there is no master curve that can represent the response of materials with different microstructures.

To account the effect of the initial porosity, a microstructure-sensitive interpretation of Eq. (6) is used. Specifically, E_c is taken as a function of the initial porosity, leading to a modified HJ relation of the form

$$1 = \frac{E_c(\eta)}{E} + \frac{\Sigma_c}{\Sigma}. \tag{7}$$

Equation (7) is fitted to the CFEM data for each initial porosity η level, as shown in Fig. 25(b). E_c is obtained as a function of η from the fit. For the range of volume fractions and impact velocities considered, Eq. (7) provides a good fit to the CFEM results. This shows that the modified HJ relation can be used to incorporate the effect of porosity (microstructure) in the description of the E-v relation.

The variation of E_c with η is shown in Fig. 26 for the three GX microstructures having initial volume fractions of $\eta = 0.60$, 0.70, and 0.82 [Figs. 5(b), 5(e), and 5(f)]. Overall, E_c increases approximately linearly with η, reflecting the fact that higher amounts of energy are absorbed by materials with higher packing densities prior to criticality in general. This can be explained by the trend in the time to criticality

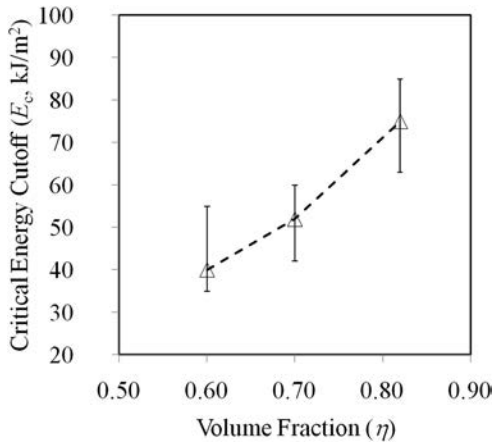

FIG. 26. Critical input energy cutoff (E_c) as a function of η for GXs with grain volume fractions between $\eta = 0.60$–0.82, the impact velocities are between $v = 50$–$250\,\mathrm{ms}^{-1}$.

(t_c) curves for different microstructures at high impact velocities [see, Figs. 23(a) and 23(b)]. Since t_c does not change significantly with porosity (at high impact velocity), the energy absorbed E_c increases with volume fraction.

1. Time to criticality and critical input energy

Along with the critical input energy, the time to criticality is another parameter associated with the behavior of energetic materials. These two parameters are not independent of each other, rather, they are related. Together, they provide two perceptives toward the same phenomenon. We now consider the time required to reach thermal runaway t_c.

For shock loading, the Rankine-Hugoniot is used to relate shock pressure to impact velocity. The shock pressure is assumed to be constant over the duration of interest. The issue is more complicated for non-shock loading. For small samples [loading configuration 1, Fig. 7(a)], the stress in the loading direction varies with time and depends on microstructure and loading rate. This requires the history of stress to be quantified.

Hayes and Mitchell[15] suggested that material response during the compaction process is similar to that in a process involving phase changes, with the following characteristics:

(1) an initial low–pressure region, where the response is elastic, followed by
(2) a mixed-phase region where crushing of granules occur, and finally,
(3) a high-pressure region where the material is fully compacted.

Figure 27(a) shows the stress (σ_{ext}) as a function of displacement (x) of the loading surface, for GX microstructures with $\eta = 0.60$, 070, and 0.82. The impact velocity is $v = 50\,\mathrm{ms}^{-1}$ and the grain size distribution is bimodal with $d = 120$–$360\,\mu\mathrm{m}$. After an initial delay up to which the stress is approximately constant, it starts to increase. In the latter stages of loading, the increase is exponential with displacement.

The relations for a GX with $\eta = 0.70$ at different impact velocities between $v = 50$ and $250\,\mathrm{ms}^{-1}$ are shown in Fig. 27(b). At low impact velocities ($v = 50 - 100\,\mathrm{ms}^{-1}$), the response is relatively less sensitive to loading rate or impact velocity, indicating that there is very little crushing of the granules upon impact. At higher impact velocities ($v \geq 150\,\mathrm{ms}^{-1}$), however, high stress levels are seen, even at low displacement levels($x < 0.4\,\mathrm{mm}$), leading to early fracture of grains and intense frictional dissipation. The stress in the low displacement regime increases with impact velocity. As seen previously in Fig. 27(a), at higher levels of overall displacement, the stress increases exponentially with displacement. To analyze the loading history for small samples with wave reflections, both regimes of the stress-displacement behavior need to be considered, since criticality can occur at either loading regime, depending on the impact velocity [see, Figs. 27(a) and 27(b)].

For different grain volume fractions, the stress-displacement relationship can be described by

$$\sigma_{ext} = \rho_0 c_0 v + \mathrm{K}\left(\frac{x}{l_0}\right)^{\gamma}, \tag{8}$$

where x is the displacement of the loading surface, ρ_0 is the effective density, c_0 is the effective initial longitudinal stress wave speed in the porous material, K is a constant, l_0 is the initial length of the specimen, and γ is a function of the initial grain volume fraction. The values of the constants are listed in Table II. For this set of calculations, it is found that $\gamma = 1/\eta^4$. Equation (8) represents the superimposition of two distinct responses of the material during loading. Specifically,

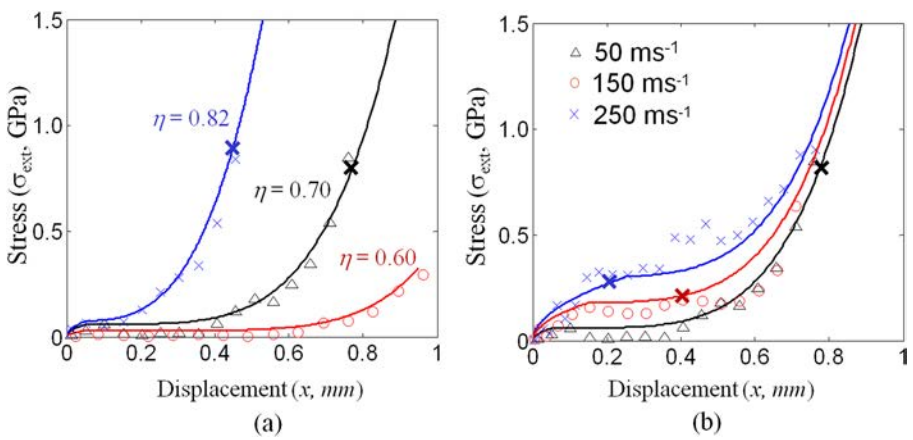

FIG. 27. Histories of stress for GXs (a) with grain volume fractions between $\eta = 0.60$–0.82 ($v = 50\,\mathrm{ms}^{-1}$ and $\dot{\varepsilon} = 16.6 \times 10^3\,\mathrm{s}^{-1}$); and (b) under loading at impact velocities between $v = 50$–$250\,\mathrm{ms}^{-1}$ ($\eta = 0.70$); the crosses show the points where criticality is reached.

TABLE II. Parameters used in Eqs. (6)–(11).

Parameter	Value	Units
K	500	GPa
l_o	3.0	mm
Σ_c	1.0	$m^2\ s^{-2}$

(1) the first term on the right-hand side is obtained from the Rankine-Hugoniot equation or the linear elastic response equation of a medium, it represents the stress generated due to the elastic response of the initially porous medium as a function of the impact velocity; and
(2) the second term represents the increase of stress due to compaction, including the effects of wave reverberations in the samples.

Figures 27(a) and 27(b) also show fits of Eq. (8) to the CFEM results. The curves appear to be able to describe the data well in the high and low velocity regimes for all volume fractions considered. Note that Eq. (8) accounts for the effects of both the impact velocity and the initial porosity. The effect of porosity is manifested through the first term (through $\rho_0 c_0$) and the second term (through parameter $\gamma = 1/\eta^4$). The variation of $\rho_0 c_0$ with η is shown in Fig. 28. Over the range of conditions analyzed, the relationship between $\rho_0 c_0$ and η is approximately linear.

The loading history [Eq. (8)] can be used to relate the critical input energy to the time to criticality to obtain a general relation of the form

$$f(v,t) = c(\eta), \tag{9}$$

where $f(v,t)$ is a function of the impact velocity and time to reach criticality. To provide an analytical evaluation of E, note that the input energy is

$$E = \int_{t=0}^{t} \sigma_{ext} dx(t), \tag{10}$$

where, t is time, σ_{ext} is the stress applied on the material, and x is the displacement of the load surface.

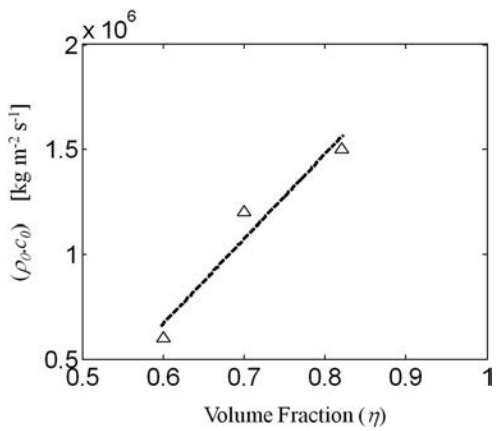

FIG. 28. Variation of $\rho_0 c_0$ for GXs with grain volume fraction.

Equation (8) can be used to derive the specific form of the v-t relation described in Eq. (9) from the modified Hugh James relation [Eq. (7)]. Specifically, integrating Eq. (8) yields a criticality condition in terms of time [as opposed to Eq. (7) which is in terms of energy]. The form is

$$\left(1 - \frac{2\Sigma_c}{v^2}\right)[1 + k(\eta) v^{1/\eta^4 - 1} t^{1/\eta^4}] v^2 t = F(E_c, \eta), \tag{11}$$

where $k(\eta)$is a function of initial porosity, $F(\cdot)$ is a function of the cutoff energy E_c, and initial porosity (see, Appendix A). The derivation of Eq. (11) is given in Appendix A. This equation incorporates the effects of microstructure, E_c and impact velocity. Note that the microstructure parameter η enters into Eq. (11) via (1) the energy flux across the impact face [Eq. (10)] and (2) the dependence of E_c on η. For the ranges of porosity and impact velocities considered in this paper, $\Sigma_c \ll v^2$, hence the approximation$(1 - 2\Sigma_c/v^2) \approx 1$ can be used in Eq. (11).

Equation (11) provides a description of the relationship between the impact velocity and time required to reach criticality for a small sample with wave reflections. It incorporates the effects of both loading and wave reflections. Figure 29 shows the time to criticality as a function of impact velocity (the v-t relation) as predicted by Eq. (11) and the corresponding CFEM data (symbols) for GX with volume fractions between $\eta = 0.60 - 0.82$. The prediction provides a reasonable description of the numerical data.

The specific form of Eq. (11) shown in Appendix A [Eq. (A4)] highlights an important aspect of the material response accounted for in the modified HJ relation. At very high velocities, the first term becomes negligible. Hence the response is dominated by the second term which strongly depends on initial porosity. On the other hand, at low impact velocities, the second term becomes negligible and the response is dominated by the first term. The response in this regime is solely dependent on the impact velocity in a manner that is similar to what is seen for shock loading. The effect of microstructure is through the effective impedance $\rho_0 c_0$.

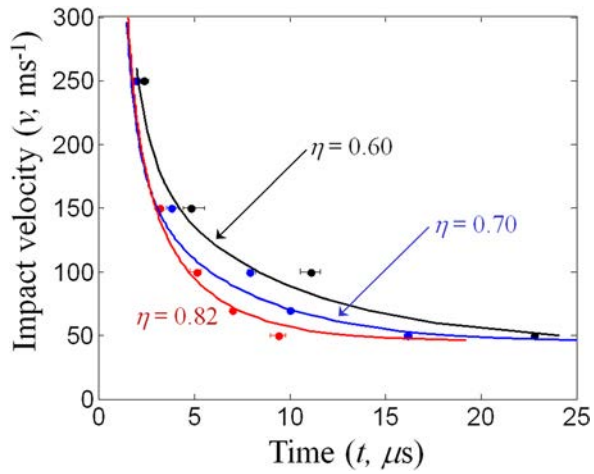

FIG. 29. Relations between time to criticality and impact velocity, CFEM data, and predictions of Eq. (11) for GX with $\eta = 0.60$–0.82 are shown.

It is important to note that the term, $k(\eta)v^{1/\eta^4-1}t^{1/\eta^4}$ in Eq. (11) accounts for the effect of multiple wave reflections. For loading without wave reflections including loading associated with the long sample configuration in Fig. 6(b) that primarily involves densification of GXs (relatively low impact velocities) and true shock loading, the second term in Eq. (8) can be neglected so that Eq. (11) reduces to the form $v^2t = c(\eta)$. This relation is equivalent to the $P^2\tau =$ constant relation proposed by Walker and Wasley[10] for shock loading, as the particle velocity and the pressure are linearly related under such conditions.

V. CONCLUSIONS

This paper has focused on two new developments.

The first is a systematic method for the characterization of hotspot fields resulting from non-shock impact loading of GXs and PBXs. This new method uses the RDF and yields quantifications of the distributions of the size and shape of hotspots and distances between hotspot as function of microstructures and loading.

The second development is a new criterion for establishing the ignition conditions of heterogeneous energetic materials under general conditions. This criterion, similar to a "yield" or failure criterion in mechanics of materials, links the hotspot size-temperature states in a loading event to the threshold size-temperature conditions of hotspots, which are regarded as materials properties. Since hotspot quantification can be explicitly obtained through simulations (CFEM in the case of this paper) or experiments regardless of loading and because threshold hotspot size-temperature pairs are material attributes, this criterion applies to both shock and non-shock conditions.

Both the hotspot quantification method and the new ignition criterion have been used to analyze the behavior of granular HMX and polymer-bonded HMX with different microstructures. For different loading configurations and materials, the study has yielded the critical impact velocity for ignition and critical time required for ignition as a function of material and impact velocity. The microstructural samples are from both real materials and systematic computations. The analysis also concerns different loading conditions (rates, wave reflections). The results show that fracture of energetic grains and subsequent friction along crack faces constitutes the most important heating mechanism in general.

For the PBXs at moderate and high impact velocities, grain fracture and friction are primarily responsible for heating. For the GXs, initial porosity plays the most important role in heating in terms of heating rate but not hot-spot size and spacing. In contrast, grain size of GX appears to have negligible influence on ignition. The effect of porosity is most pronounced at low impact velocities and negligible at high impact velocities when localized fracture and friction near impact face dominate.

Wave reflections from confined boundaries (associated with small samples and larger impactors) multiply stress and temperature increases, making even low velocity impact dangerous if loading is maintained over sufficiently long durations. While for large samples (no wave reflections), GX is more susceptible to ignition at all impact velocities. For small, confined samples, GX is more susceptible at high impact velocities, while PBX is more susceptible at low impact velocities, when deformed to the same level of total strain. For the range of impact velocities considered, PBX is 2–4 times safer (in terms of critical impact velocity) than HMX at high impact velocities.

The applicability of the critical input energy (E) relation proposed by James[2] for non-shock loading is examined, leading to a modified relation, which is sensitive to microstructure and loading. The modified relation accounts for the variation of E_c with porosity. The relation in the v-t space accounts for the effects of both the input stress wave (compaction of material) and the reflection of the stress wave. Under the effect of the input wave only without reflections, the relation reduces to the $P^2\tau =$ constant relation of Walker and Wasley.[10]

It is important to reiterate that, although the ignition criterion proposed in this paper in theory applies to both non-shock and shock loading, the analyses so far have exclusively focused on non-shock conditions. The application to shock loading should be discussed in the future with appropriately configured computational calculations and experimental measurements of hotspot fields.

As a final observation, it must be mentioned that the stochastic nature of microstructural heterogeneities such as varying grain size and random constituent morphologies necessitate a statistical approach in the quantification of hotspot formation and the application of the ignition criterion developed here. Consequently, the issue of hotspot criticality needs to be further analyzed from a probabilistic viewpoint. This is the subject of ongoing research and shall appear in a future publication.

ACKNOWLEDGMENTS

The authors gratefully acknowledge support from the Air Force Research Laboratory (AFRL) at the Eglin AFB in Florida and the Defense Threat Reduction Agency (DTRA) (scientific officer: Dr. Suhithi Peiris). Calculations are carried out on parallel computers at NAVO and the DPRL at Georgia Tech.

APPENDIX: DERIVATION OF CRITICALITY CONDITION [EQ. (11)].

Equation (10) can also be rewritten as

$$E = \int_{x=0}^{x} \sigma_{ext} dx. \tag{A1}$$

The stress-displacement relation in Eq. (8) can be substituted into Eq. (A1) to obtain the critical input energy E as

$$E = \int_{x=0}^{x} \left(\rho_0 c_0 v + \mathrm{K}\left(\frac{x}{l_0}\right)^{\gamma} \right) dx. \tag{A2}$$

Substituting $x = v$t (for a constant boundary velocity, v) into the above expression and integrating yield

$$E = \rho_0 c_0 v^2 t + \frac{K}{(\gamma+1) l_0^{\gamma}} (vt)^{(\gamma+1)}. \tag{A3}$$

If we use the HJ relation in the form of Eq. (7), the critical condition can be expressed as

$$1 = \frac{2\Sigma_c}{v^2} + \frac{E_c}{\rho_0 c_0 v^2 t + \frac{K}{(\gamma+1) l_0^{\gamma}} (vt)^{(\gamma+1)}}. \tag{A4}$$

This relation can be recast into the more convenient form of

$$\left(1 - \frac{2\Sigma_c}{v^2}\right)[1 + k(\eta) v^{1/\eta^4 - 1} t^{1/\eta^4}] v^2 t = F(\eta), \tag{A5}$$

where

$$\begin{cases} k(\eta) = \dfrac{K}{\left(\dfrac{1}{\eta^4} + 1\right) \rho_0 c_0 l_0^{\frac{1}{\eta^4}}}, \\ \text{and} \quad F(\eta) = \rho_0 c_0 E_c(\eta). \end{cases} \tag{A6}$$

Note that in Eqs. (A2)–(A6), $\rho_0 c_0$ is a function of η, as shown in Fig. 28.

[1] C. M. Tarver, S. K. Chidester, and A. L. Nichols, "Critical conditions for impact- and shock-induced hot spots in solid explosives," J. Phys. Chem. **100**, 5794–5799 (1996).
[2] H. R. James, "An extension to the critical energy criterion used to predict shock initiation thresholds," Propellants, Explos., Pyrotech. **21**, 8–13 (1996).
[3] M. R. Baer, "Modeling heterogeneous energetic materials at the mesoscale," Thermochimica Acta **384**, 351–367 (2002).
[4] J. E. Field, "Hot-spot ignition mechanisms for explosives," Acc. Chem. Res. **25**, 489–496 (1992).
[5] R. Menikoff, "Pore collapse and hot spots in HMX," in *Shock Compression of Condensed Matter—2003, Pts 1 and 2, Proceedings*, edited by M. D. Furnish *et al*. (AIP, Melville, 2004), Vol. 706, pp. 393–396.
[6] Y. Hamate and Y. Horie, "Ignition and detonation of solid explosives: A micromechanical burn model," Shock Waves **16**, 125–147 (2006).
[7] B. Asay, *Non-Shock Initiation of Explosives Non-Shock Initiation of Explosives* (Springer-Verlag, Berlin, 2010).
[8] P. A. Urtiew and C. M. Tarver, "Shock initiation of energetic materials at different initial temperatures (review)," Combust., Explos. **41**, 766–776 (2005).
[9] H. L. Berghout, S. F. Son, C. B. Skidmore, D. J. Idar, and B. W. Asay, "Combustion of damaged PBX 9501 explosive," Thermochim. Acta **384**, 261 (2002).
[10] F. E. Walker and R. J. Wasley, "Critical energy for shock initiation of heterogeneous explosives," Explosivstoffe **17**, 9 (1969).
[11] M. R. Baer, C. A. Hall, R. L. Gustavsen, D. E. Hooks, and S. A. Sheffield, "Isentropic loading experiments of a plastic bonded explosive and constituents," J. Appl. Phys. **101**, 12 (2007).
[12] W. M. Trott, M. R. Baer, J. N. Castaneda, L. C. Chhabildas, and J. R. Asay, "Investigation of the mesoscopic scale response of low-density pressings of granular sugar under impact," J. Appl. Phys. **101**, 024917 (2007).
[13] R. A. Austin, D. L. McDowell, and D. J. Benson, "Numerical simulation of shock wave propagation in spatially resolved particle systems," Model. Simul. Mater. Sci. Eng. **14**, 537–561 (2006).
[14] D. J. Benson and P. Conley, "Eulerian finite-element simulations of experimentally acquired HMX microstructures," Model. Simul. Mater. Sci. Eng. **7**, 333–354 (1999).
[15] D. B. Hayes and D. E. Mitchell, *Constitutive Equation for the Shock Response of Porous Hexanitrostilbene (HNS) Explosive* (Symposium on High Pressures, Paris, France, 22 Aug, 1978).
[16] R. Menikoff, *Compaction Wave Profiles in Granular HMX, 1999 27 June–2 July* (Los Alamos National Laboratory, Los Alamos, NM), AIP Conf. Proc. **505**, pp. 397–400.
[17] R. Menikoff, "Granular explosives and initiation sensitivity," *LA-UR-99-6023, IMA Workshop on Combustion of Energetic Materials*, November 1999, http://lib-www.lanl.gov/la-pubs/00796456.pdf.
[18] H. Kim, A. Lagutchev, and D. D. Dlott, "Surface and interface spectroscopy of high explosives and binders: HMX and Estane," Propellants, Explos., Pyrotech. **31**, 116–123 (2006).
[19] A. Tokmakoff, M. D. Fayer, and D. D. Dlott, "Chemical-reaction initiation and hot-spot formation in shocked energetic molecular materials," J. Phys. Chem. **97**, 1901–1913 (1993).
[20] B. F. Henson, B. W. Asay, L. B. Smilowitz, and P. M. Dickson, "Ignition chemistry in HMX from thermal explosion to detonation," in *Shock Compression of Condensed Matter-2001, Pts 1 and 2, Proceedings*, edited by M. D. Furnish *et al*. (2002), Vol. 620, pp. 1069–1072.
[21] D. J. Idar, J. W. Straight, M. A. Osborn, C. B. Skidmore, D. S. Phillips, and G. A. Buntain, "PBX 9501 high explosive violent reaction: Phase II baseline and aged experiments," Los Alamos National Laboratory Report No. LA-13641-MS, 2000, http://www.fas.org/sgp/othergov/doe/lanl/lib-www/la-pubs/00538217.pdf.
[22] G. T. Gray III, W. R. Bluementhal, D. J. Idar, and C. M. Cady, "Influence of temperature on the high strain-rate mechanical behavior of PBX 9501," *Shock Compression of Condensed Matter—1997*, edited by S. C. Schmidt, D. P. Dandekar, and J. W. Forbes (1998), pp. 583–586.
[23] J. K. Dienes, Q. H. Zuo, and J. D. Kershner, "Impact initiation of explosives and propellants via statistical crack mechanics (Vol. 54, p. 1237, 2006)," J. Mech. Phys. Solids **54**, 2235–2240 (2006).
[24] R. Panchadhara and K. A. Gonthier, "Mesoscale analysis of volumetric and surface dissipation in granular explosive induced by uniaxial deformation waves," Shock Waves **21**, 43–61 (2011).
[25] A. Barua and M. Zhou, "A Lagrangian framework for analyzing microstructural level response of polymer-bonded explosives," Model. Simul. Mater. Sci. Eng. **19**, 24 (2011).
[26] A. Barua, Y. Horie, and M. Zhou, "Energy localization in HMX-Estane polymer-bonded explosives during impact loading," J. Appl. Phys. **111**, 11 (2012).
[27] A. Barua and M. Zhou, "Computational analysis of temperature rises in microstructures of HMX-Estane PBXs," Comput. Mech. 1–9 (2012).
[28] Y. Q. Wu and F. L. Huang, "A microscopic model for predicting hot-spot ignition of granular energetic crystals in response to drop-weight impacts," Mech. Mater. **43**, 835–852 (2011).
[29] R. V. Browning and R. J. Scammon, "Microstructural model of ignition for time varying loading conditions," in *Shock Compression of Condensed Matter-2001, Pts 1 and 2, Proceedings*, edited by M. D. Furnish *et al*. (AIP, Melville, 2002), Vol. 620, pp. 987–990.
[30] N. Semenov, Zeitschrift für Physik, Z. Phys. **48**(7-8), 571–582 (1928).
[31] D. A. Kamenetskii, Zh. Fiz. Khim. **13** (1939).
[32] P. H. Thomas, "On the thermal conduction equation for self-heating materials with surface cooling," Trans. Faraday Soc. **54**, 60–65 (1958).
[33] P. Gray and J. C. Lee, "The combustion of gaseous hydraziene," Trans. Faraday Soc. **50**, 719–728 (1954).
[34] P. Gray and P. R. Lee, "Thermal explosions and effect of reactant consumption on critical conditions," Combust. Flame **9**, 201 (1965).
[35] T. Boddington, P. Gray, W. Kordylewski, and S. K. Scott, "Thermal explosions with extensive reactant consumption—A new criterion for criticality," in *Proceedings of the Royal Society of London Series a-Mathematical Physical and Engineering Sciences* (1983), Vol. 390, pp. 13–30.
[36] T. Boddington, P. Gray, and G. C. Wake, "Criteria for thermal explosions with and without reactant consumption," in *Proceedings of the Royal Society of London Series a-Mathematical Physical and Engineering Sciences* (1977), Vol. 357, pp. 403–422.
[37] J. Zhai, V. Tomar, and M. Zhou, "Micromechanical simulation of dynamic fracture using the cohesive finite element method," Trans. ASME J. Eng. Mater. Technol. **126**, 179–191 (2004).
[38] V. Tomar, J. Zhai, and M. Zhou, "Bounds for element size in a variable stiffness cohesive finite element model," Int. J. Numer. Methods Eng. **61**, 1894–1920 (2004).
[39] E. M. Mas and B. E. Clements, "A viscoelastic model for PBX binders," Los Alamos Internal Report: (LA-UR-01-3492) 1996), http://lib-www.lanl.gov/la-pubs/00818442.pdf.
[40] H. E. Alper and P. Politzer, "Molecular dynamics simulations of the temperature-dependent behavior of aluminum, copper, and platinum," Int. J. Quantum Chem. **76**, 670–676 (2000).
[41] B. H. Zimm, "The scattering of light and the radial distribution function of high polymer solutions," J. Chem. Phys. **16**, 1093–1099 (1948).

[42]G. Mason, "Radial distribution functions from small packing of spheres," Nature **217**, 733 (1968).
[43]G. X. Li, Y. F. Liang, Z. G. Zhu, and C. S. Liu, "Microstructural analysis of the radial distribution function for liquid and amorphous Al," J. Phys. Condens. Matter **15**, 2259–2267 (2003).
[44]M. R. Baer, D. K. Gartling, and P. E. DesJardin, "Probabilistic models for reactive behaviour in heterogeneous condensed phase media," Combust. Theory Modell. **16**, 75–106 (2012).
[45]C. R. Siviour, P. R. Laity, W. G. Proud, J. E. Field, D. Porter, P. D. Church, P. Gould, and W. Huntingdon-Thresher, "High strain rate properties of a polymer-bonded sugar: their dependence on applied and internal constraints," Proc. R. Soc. London, Ser. A **464**, 1229–1255 (2008).
[46]A. Barua, Y. Horie, and M. Zhou, "Microstructural level response of HMX–Estane polymer-bonded explosive under effects of transient stress waves," Proc. R. Soc. London, Ser. A **468**, 3725–3744 (2012).
[47]J. J. Dick, A. R. Martinez, and R. S. Hixson, *Plane Impact Response of Pbx 9501 and its Components Below 2 Gpa* (Los Alamos National Lab., NM, 1998).
[48]A. G. Xu, G. C. Zhang, P. Zhang, X. F. Pan, and J. S. Zhu, "Dynamics and thermodynamics of porous HMX-like material under shock," Commun. Theor. Phys. **52**, 901–908 (2009).
[49]S. D. Herring, T. C. Germann, and N. Gronbech-Jensen, "Effects of void size, density, and arrangement on deflagration and detonation sensitivity of a reactive empirical bond order high explosive," Phys. Rev. B **82**, 214108 (2010).
[50]R. W. Armstrong, C. S. Coffey, V. F. Devost, and W. L. Elban, "Crystal size dependence for impact initiation of cyclotrimethylenetrinitramine explosive," J. Appl. Phys. **68**, 979–984, (1990).
[51]H. Czerski and W. G. Proud, "Relationship between the morphology of granular cyclotrimethylene-trinitramine and its shock sensitivity," J. Appl. Phys. **102**, 113515 (2007).
[52]P. M. Howe, R. B. Frey, B. Taylor, and V. Boyle, "Shock initiation and the critical energy concept," in *Sixth Symposium (International) on Detonation* (1976), pp. 11–19.
[53]S. Lecume, C. Spyckerelle, and F. Sommer, "Structure of pristine crystal defects revealed by AFM and microtomography," AIP Conf. Proc. **706**, 997–1000 (2004).
[54]A. Chakravarty, M. J. Gifford, M. W. Greenaway, W. G. Proud, and J. E. Field, "Factors affecting shock sensitivity of energetic materials," in *Shock Compression of Condensed Matter-2001, Pts 1 and 2, Proceedings*, edited by M. D. Furnish *et al*. (2002), Vol. 620, pp. 1007–1010.
[55]H. R. James, "Shock initiation thresholds for insensitive high explosives," in *Shock Compression of Condensed Matter—2007, Pts 1 and 2*, edited by M. Elert *et al*. (AIP, Melville, 2007), Vol. 955, pp. 937–940.
[56]H. R. James, R. J. Haskins, and M. D. Cook, "Prompt shock initiation of cased explosives by projectile impact," Propellants, Explos., Pyrotech. **21**, 251–257 (1996).